

# An Intermediate-band imaging survey for high-redshift Lyman Alpha Emitters: The Mahoroba-11

Sanae F. YAMADA,<sup>1</sup> Shunji S. SASAKI,<sup>1</sup> Ryoko SUMIYA,<sup>1</sup> Kazuyoshi UMEDA,<sup>1</sup>  
 Yasuhiro SHIOYA,<sup>1</sup> Masaru AJIKI<sup>1</sup>, Tohru NAGAO,<sup>2,3</sup>  
 Takashi MURAYAMA,<sup>1</sup> and Yoshiaki TANIGUCHI<sup>1</sup>

*shioya@astr.tohoku.ac.jp*

*tani@astr.tohoku.ac.jp*

<sup>1</sup>*Astronomical Institute, Graduate School of Science, Tohoku University,  
 Aramaki, Aoba, Sendai 980-8578*

<sup>2</sup>*National Astronomical Observatory of Japan,  
 2-21-1 Osawa, Mitaka, Tokyo 181-8588*

<sup>3</sup>*INAF — Osservatorio Astrofisico di Arcetri,  
 Largo Enrico Fermi 5, 50125 Firenze, Italy*

(Received 2005 January 0; accepted 0 0)

## Abstract

We present results of our intermediate-band optical imaging survey for high- $z$  Ly $\alpha$  emitters (LAEs) using the prime focus camera, Suprime-Cam, on the 8.2m Subaru Telescope. In our survey, we use eleven filters; four broad-band filters ( $B$ ,  $R_c$ ,  $i'$ , and  $z'$ ) and seven intermediate-band filters covering from 500 nm to 720 nm; we call this imaging program as the Mahoroba-11. The seven intermediate-band filters are selected from the IA filter series that is the Suprime-Cam intermediate-band filter system whose spectral resolution is  $R = 23$ . Our survey has been made in a  $34' \times 27'$  sky area in the Subaru XMM Newton Deep Survey field. We have found 409 IA-excess objects that provide us a large photometric sample of strong emission-line objects. Applying the photometric redshift method to this sample, we obtained a new sample of 198 LAE candidates at  $3 < z < 5$ . We found that there is no evidence for evolution of the number density and the star formation rate density for LAEs with  $\log L(\text{Ly}\alpha)(\text{erg s}^{-1}) > 42.67$  between  $z \sim 3$  and 5.

**Key words:** cosmology: observations — early universe — galaxies: formation — galaxies: evolution

## 1. Introduction

Formation and evolution of galaxies have been intensively discussed in this decade. This progress has been supported by the Hubble Space Telescope (HST) and ground-based 8-10 m class telescopes such as the W. M. Keck telescopes, VLT, the Gemini Telescopes, and the Subaru Telescope. In particular, the Hubble Deep Fields (Williams et al. 1996, 2000) and the Hubble Ultra Deep Field (Beckwith et al. 2003) make it possible to search for very faint galaxies beyond  $z = 5$  (e.g., Lanzetta et al. 1996; Weymann et al. 1998; Bunker et al. 2004; Yan, Windhorst 2004).

Early star formation in galaxies could occur beyond  $z = 5$  (e.g., see for reviews, Taniguchi et al. 2003b, Spinrad 2003). Yet, the peak of star formation in the universe appears to occur at  $z \sim 1$  (Madau et al. 1996; Steidel et al. 1999; Ouchi et al. 2004; Giavalisco et al. 2004). Although this observational trend has been widely accepted, we have not yet fully understood which physical processes play crucially important roles during the course of evolution of galaxies. Therefore, in order to understand the whole history of galaxies in the universe from high redshift to the present day, it is important to carry out systematic searches for galaxies at any redshift.

It has been also claimed that the basic dynamical properties of galaxies could be determined at  $1 < z < 3$ ; i.e., the origin of the Hubble type of galaxies could be established at this redshift interval (e.g., Kajisawa, Yamada 2001). In addition, early star formation in galaxies as well as early growth of supermassive black holes in their nuclei should be clarified unambiguously in terms of the hierarchical structure formation paradigm (Madau et al. 1996; Barger et al. 2001; Kauffmann, Haehnelt 2000).

In order to explore this issue, it is absolutely necessary to investigate observational properties of galaxies beyond  $z = 1$ . Indeed, many observational programs have been devoted to this problem by finding high- $z$  galaxies. Searches for such high- $z$  galaxies have been carried out mainly by the following two methods. One is the optical broad-band color selection technique (e.g., Steidel, Hamilton 1992; Steidel et al. 1999; Madau et al. 1996; Lanzetta et al. 1996; Giavalisco et al. 2004 and references therein). The other method is deep searches for strong Ly $\alpha$  emitters by using an optical narrow-band filter (Hu et al. 1996; Cowie, Hu 1998; Kudritzki et al. 2000; Rhoads et al. 2000; Ajiki et al. 2003; Kodaira et al. 2003; Taniguchi et al. 2005). We also note that the slitless grism spectroscopy is another method to search for the high- $z$  galaxies (Kurk et al. 2004; Martin & Sawicki 2004; Pirzkal et al. 2004).

The first method provides a relatively large sample of high- $z$  Lyman break galaxies (LBGs) and their follow-up spectroscopy tells us global properties of high- $z$  galaxies. However, such studies are biased to investigations of relatively bright galaxies because a certain magnitude-limited sample is used in such a study. On the other hand, the second method provides us a sample of strong emission-line objects, most of which are missed in a magnitude-limited sample, although it is not clear whether or not they are typical faint normal galaxies.

However, because of the narrowness of the filter bandpass, such a study can only probe strong emission-line objects in a small volume of the universe (see for a review, Taniguchi et al. 2003b).

In order to overcome the demerit of searches with a narrow-band filter, searches with multi narrow-band filters have been made in some cases (Rhoads et al. 2000; Shimasaku et al. 2004). Even in their pioneering surveys, only a couple of filters were used and thus their survey volumes were still small. More recently, new surveys with a combination between typical broad-band filters and intermediate- and narrow-band filters have been conducted. The most successful survey made so far is the COMBO-17 survey in which 17 filters are used (Wolf et al. 2003a; see also Bell et al. 2004); 5 broad-band filters and 12 medium-band ones. Indeed, this survey has been used to make a systematic search for strong emission-line objects such as active galactic nuclei between  $z \sim 1$  and  $z \sim 5$  (Wolf et al. 2003b).

In order to search for strong Ly $\alpha$  emitters systematically, we have conducted a new deep optical imaging survey with 11 filters using the prime focus camera, Suprime-Cam (Miyazaki et al. 2002), on the 8.2m Subaru Telescope (Kaifu et al. 2000; Iye et al. 2004). In this survey, we use a set of seven intermediate-band (IA) filters covering wavelengths from  $\approx 527\text{nm}$  to  $709\text{nm}$ , corresponding to the Ly $\alpha$  redshift from  $z = 3.4$  and  $z = 4.8$  (Hayashino et al. 2000; Taniguchi 2004; Fujita et al. 2003; Taniguchi et al. 2003b; Ajiki et al. 2004). This new data set allows us to investigate the cosmic star formation history systematically from  $z = 4.8$  to  $z = 3.3$  for the first time. In this paper, we present our results and then discuss the nature of strong Ly $\alpha$  emitters at high redshift.

Throughout this paper, we adopt a flat universe with  $\Omega_m = 0.3$ ,  $\Omega_\Lambda = 0.7$ , and  $H_0 = 70 \text{ km s}^{-1}\text{Mpc}^{-1}$ , and we use the AB magnitude system (e.g. Oke 1974).

## 2. Observations and data reduction

### 2.1. Observations

Deep and wide-field  $B$ -,  $R$ -,  $i'$ -, and  $z'$ -band imaging data of a southward  $30' \times 24'$  area in the Subaru/XMM-Newton Deep Survey Field (the SXDS field<sup>1</sup>) centered at  $\alpha(\text{J2000}) = 2^{\text{h}}18^{\text{m}}00^{\text{s}}$  and  $\delta(\text{J2000}) = -5^\circ12'00''$  were obtained using the Suprime-Cam (Miyazaki et al. 2002) on the 8.2m Subaru Telescope during a period between 2000 August, and 2002 January by the SXDS team. The Suprime-Cam consists of ten CCD chips, each of which has  $2048 \times 4096$  pixels, providing a field of view of  $27' \times 34'$ .

In the SXDS field, X-ray deep survey by the XMM-Newton satellite as well as multi-broad-band imaging observations are on-going over 1.3 square degree area. Therefore, the field is one of the most suitable target fields for our IA filter survey. Carefully examining the entire SXDS field, we selected the southward field of SXDS field which do not contain any bright stars. Note that a sky area of  $13.^{\circ}7 \times 13.^{\circ}7$  in the central part of the SXDS field was already

---

<sup>1</sup> See <http://www.naoj.org/Science/SubaruProject/SDS/>.

observed by Fujita et al. (2003) using an IA filter, *IA*574. However, our observing field does not overlap with it (see figure 2).

In addition to these broad-band image data, intermediate-band images were obtained during an open-use observing program, S02B-163 (PI = K. Kodaira), using the following IA filters: *IA*527, *IA*574, *IA*598, *IA*624, *IA*651, *IA*679, and *IA*709, on Suprime-Cam / Subaru Telescope during a period between 2002 October and 2002 November. The center wavelength and *FWHM* of these IA filters are summarized in table 1; see also <http://www.awa.tohoku.ac.jp/~tamura/astro/filter.html>, Hayashino et al. (2000, 2003), and Taniguchi (2001). The transmission curves of the filters used in our observations are shown in figure 1. A journal of our all observations is given in table 1. All of the observations were made under photometric conditions, and the seeing size was  $\simeq 1.^{\prime\prime}0$ .

## 2.2. Data Reduction

The individual CCD data were reduced and combined using IRAF and the mosaic-CCD data reduction software developed by Yagi et al. (2002). The following spectrophotometric standard stars were observed to calibrate the IA filter imaging data; LDS749B, LTT9491, G93-48, and Feige110 [references here Oke (1974), Oke (1990), Landolt (1992), and Stone (1996)]. The combined images for the individual bands were aligned and smoothed with Gaussian kernels to match their seeing sizes. The final images cover a contiguous 944 arcmin<sup>2</sup> area ( $34.^{\circ}71 \times 27.^{\circ}20$ ) with a PSF FWHM of  $1.^{\prime\prime}04$  for the broad-band and IA-band data. The final IA image stacked with the seven IA images is shown in figure 3. After masking out areas which are affected by the starlight, we obtained the final image whose effective sky coverage is 526 arcmin<sup>2</sup>. Note that the data reduction was made by the team of S02B-163 program in which the authors in this paper were included as collaborators.

## 3. Results

### 3.1. Source Detection and Photometry

For photometry and source detection of our observational data, we use SExtractor version 2.1.7 (Bertin & Arnouts 1996). As for the source detection in all images, we use the limiting magnitudes for a  $3\sigma$  detection with a  $2''$  diameter aperture :  $B = 28.2$ ,  $R_c = 27.4$ ,  $i' = 27.0$ ,  $z' = 25.8$ ,  $IA527 = 26.8$ ,  $IA574 = 26.5$ ,  $IA598 = 26.5$ ,  $IA624 = 26.7$ ,  $IA651 = 26.7$ ,  $IA679 = 26.8$ , and  $IA709 = 26.6$ . In the above source detection, we have detected  $\sim 70000$  sources down to  $IA = 27$  in each IA image.

As shown in the left panel of figure 4, we can detect objects to  $\sim 27$  mag with above condition. In order to examine the completeness of our IA images, we show results of the number counts in the IA imaging as a function of AB magnitude in figure 4. These results show that our IA imaging appears complete down to 26.5 – 27 mag for each IA image.

In order to examine further how accurately we select emission-line objects in our IA

images, we have made simulations using IRAF ARTDATA (e.g., Kajisawa et al. 2000; Fujita et al. 2003). For this purpose, we generate two sets of 300 model galaxies for each magnitude interval,  $\Delta m = 0.2$  mag. Model galaxies in the first set obey the de Vaucouleurs  $r^{1/4}$  law light distribution while those in the second set obey the exponential law. Their sky positions, half-light radius (from 1 to 7 kpc), and ellipticities are randomly determined. We put these galaxies into the CCD data together with Poisson noises. After smoothing model-galaxy images to match to the seeing size of our observation, we try to detect them using SExtractor with the same procedure as that we used in our reduction. In the right panel of figure 4, the detectability is shown as a function of IA magnitude for each IA filter. These results also show that our IA imaging appears complete down to 26.5 – 27 mag for each IA image.

### 3.2. Selection of IA-Excess Objects

We describe our procedures to select IA-excess objects from our data set. For this purpose, we need a continuum image for each IA image. Since the central wavelength of each IA filter does not generally match to that of a certain broad band filter, we have to generate a custom continuum image for each IA filter. In previous studies (e.g., Steidel et al. 2000; Fujita et al. 2003), the broad band image whose effective wavelength is close to that of the concerned narrow-band or intermediate-band one was used as a continuum image. However, if we follow this way, continuum break objects such as LBGs could also be selected as a strong IA-excess object. In order to reject such objects, we have adopted the image of the broad filter band ( $D[IA]$ ) whose central wavelength is longer than that of the concerned IA filter as a continuum image:  $D[IA]$  is  $R_c$ -band for  $IA527$ ,  $IA574$ , and  $IA598$ , and  $i'$ -band for  $IA624$ ,  $IA651$ ,  $IA679$ , and  $IA709$ . Hereafter, we refer these continuum  $D[IA]$ , or  $D[IA_{nnn}]$  where  $nnn = 527, 574, 598, 624, 651, 679$ , or  $709$ .

In figure 5, we show the color - magnitude diagram between  $D[IA] - IA$  and  $IA$  for objects in our  $IA$  catalogs. Taking the scatter in the  $D[IA] - IA$  color into account, we define strong IA-excess objects with the following criterion,

$$D[IA] - IA \geq \text{mag}(EW_{\text{rest}} = 20\text{\AA}), \quad (1)$$

where  $\text{mag}(EW_{\text{rest}} = 20\text{\AA})$  is the magnitude corresponding to  $EW_{\text{rest}} = 20\text{\AA}$  determined as,

$$D[IA] - IA = -2.5 \log \frac{FWHM(IA)}{EW_{\text{obs}} + FWHM(IA)}, \quad (2)$$

where  $FWHM(IA)$  is the  $FWHM$  of IA filter (see table 1).  $\text{mag}(EW_{\text{rest}} = 20\text{\AA})$  are 0.332, 0.325, 0.314, 0.320, 0.311, 0.311, and 0.339 for  $IA527$ ,  $IA574$ ,  $IA598$ ,  $IA624$ ,  $IA651$ ,  $IA679$ , and  $IA709$ , respectively. These criteria are shown by horizon lines in figure 5. We also add the criteria for error,

$$D[IA] - IA > 3\sigma(D[IA] - IA) \quad \text{and} \quad IA < 3\sigma(IA) \quad (3)$$

(see curved lines in figure 5). Then, we select 74, 47, 42, 48, 60, 77, and 61 strong IA-

excess objects in the *IA*527, *IA*574, *IA*598, *IA*624, *IA*651, *IA*679, and *IA*709 filter images, respectively.

### 3.3. Selection of Lyman $\alpha$ Emitter Candidates

Because of the large observed equivalent width, it seems that most IA-excess objects may be LAEs at high redshift. However, there may be still a possibility that some of them are strong emission-line objects at lower redshifts; e.g., H $\alpha$  emitters at  $z \sim 0.00$  to 0.10, [O III]  $\lambda 5007$  emitters at  $z \sim 0.03$  to 0.45, and [O II]  $\lambda 3727$  emitters at  $z \sim 0.38$  to 0.94. Here, we try to select LAEs from IA-excess objects. Although a color - color diagram is usually used to separate the LAEs from low-z emission-line galaxies (e.g., Taniguchi et al. 2005), it seems difficult to separate LAEs properly especially for blue IA bands. We therefore adopt the photometric redshift (SED fitting) technique using all 11 bands photometric data. Using this method, we can select LAEs with enough accuracy for all IA bands. The detailed discussion on the accuracy of the photometric redshift is shown in appendix 1.

For this purpose, we generate model galaxy SEDs using the population synthesis model, GALAXEV, developed by Bruzual & Charlot (2003). The SEDs of local galaxies are well reproduced by models whose star-formation rate declines exponentially (the  $\tau$  model) : i.e.,  $SFR(t) \propto \exp(-t/\tau)$ , where  $t$  is the age of galaxy and  $\tau$  is the time scale of star formation. In this study, we use  $\tau = 1$  Gyr models with Salpeter's initial mass function (the power index of  $x = 1.35$  and the stellar mass range of  $0.1 \leq m/M_{\odot} \leq 100$ ) to derive various SED types. We note that the SED templates derived by Coleman et al. (1980) for elliptical galaxies, Sbc, Scd, Irr, and SB, correspond to those using  $t=8, 4, 3, 2$ , and 1 Gyr, respectively. We calculate SEDs with ages of  $t=0.1, 0.5, 1, 2, 3, 4$ , and 8 Gyr.

When we use only optical broad band photometry for estimates of the photometric redshift, we need not seriously take account of the contribution of emission lines to the broad band flux. However, in our case, we cannot neglect the contribution of some strong emission lines because our photometric data contain intermediate-band data. In order to include possible emission-line fluxes into our models, we calculate the number of ionizing photons,  $N_{\text{Lyc}}$ , from the SED which is calculated from the above population synthesis model. Then we can estimate H $\beta$  luminosity,  $L(\text{H}\beta)$  using the following formula (Leitherer & Heckman 1995),

$$L(\text{H}\beta) = 4.76 \times 10^{-13} N_{\text{Lyc}} \text{ erg s}^{-1}. \quad (4)$$

Other strong emission-line luminosities, such as for [O II], [O III], H $\alpha$ , and so on, are estimated by typical line ratios relative to H $\beta$  (PEGASE: Fioc & Rocca-Volmerange 1997).

In addition to the contribution of strong emission lines to SEDs, we also take the following two effects into account in SED templates. One is the absorption by interstellar medium in a galaxy itself. For this correction, we use the starburst reddening curve of Calzetti et al. (2000),

$$F_i(\lambda) = F_o(\lambda) 10^{0.4E_s(B-V)k'(\lambda)}, \quad (5)$$

where  $F_i(\lambda)$  is the intrinsic stellar continuum,  $F_o(\lambda)$  is the observed stellar continuum, and  $k'(\lambda) = A'(\lambda)/E_s(B-V)$  is the starburst reddening curve. The expression of  $k'(\lambda)$  is

$$\begin{aligned} k'(\lambda) &= 2.659(-1.857 + 1.040/\lambda) + R'_V \quad \text{for } 0.63\mu\text{m} \leq \lambda \leq 2.20\mu\text{m}; \\ &= 2.659(-2.156 - 1.509/\lambda - 0.198/\lambda^2 + 0.011/\lambda^3 + R'_V) \\ &\quad \text{for } 0.12\mu\text{m} \leq \lambda < 0.63\mu\text{m}, \end{aligned} \quad (6)$$

where  $R'_V = A'(V)/E_s(B-V) = 4.05$ . And another effect is the absorption from intergalactic gas. Following the method in Madau et al. (1996), we describe the observed mean specific flux of a source at redshift  $z_{\text{em}}$  as

$$\langle f(\nu_{\text{obs}}) \rangle = \frac{(1+z_{\text{em}})L(\nu_{\text{em}})}{4\pi d_L^2} \langle e^{-\tau} \rangle, \quad (7)$$

where  $\nu_{\text{obs}} = \nu_{\text{em}}/(1+z_{\text{em}})$ ,  $d_L$  is the luminosity distance corresponding to  $z_{\text{em}}$  and  $\langle e^{-\tau} \rangle$  is the average transmission.

Then, we try to fit the observed SEDs of IA-excess objects using SED templates generated by the above procedures. In this fitting, we calculate the standardized “relative likelihood” between  $z_{\text{ph}}=0$  and  $z_{\text{ph}}=5.0$ . We adopt a redshift of the primary peak of likelihood as the most probable photometric redshift only when the peak value is higher by a factor of two than that of the secondary peak. Otherwise, we judge that we cannot obtain any reliable photometric redshift. In this way, we have obtained photometric redshifts for 64, 40, 20, 26, 16, 17, and 15 LAEs found in IA527, IA574, IA598, IA624, IA651, IA679, and IA709 selected catalogs, respectively. We summarize the number of LAEs in table 2. The photometric catalogs of LAEs are shown in table 3.

We show the spatial distributions of LAEs in figure 6. The areas shown by grey color are the masked region. Although it is interesting to investigate clustering properties of these objects, a significant part of the sky area is masked on each IA image and thus it seems difficult to obtain a firm result on the clustering properties. Therefore, we do not discuss this issue further in this paper.

### 3.4. Equivalent Widths

We show the distributions of observed equivalent widths,  $EW_{\text{obs}}$ , for the high- $z$  LAE sample found in the previous section for those found in each IA filter in figure 7. We note that a LAE found in IA574 catalog have very large  $EW_{\text{obs}}$ ;  $6840.6 \text{ \AA}^2$ . These data are not shown in figure 7. We find that LAEs with smaller  $EW_{\text{obs}}$  tend to be more populous. We also show the histograms for the total sample in the lower-right panel of figure 7. Next, we show the distributions of rest-frame equivalent widths for the same samples in figure 8 where  $EW_0(\text{Ly}\alpha)$

---

<sup>2</sup> We comment on this large  $EW_{\text{obs}}$ . The  $R_c$ -band flux of this object is smaller than  $2\sigma$ . Using the  $2\sigma$  flux, we derive the lower limit of  $EW_{\text{obs}} = 1288 \text{ \AA}$ .

$$= EW_{\text{obs}}(\text{Ly}\alpha)/(1+z).$$

### 3.5. Lyman $\alpha$ luminosity

We estimate the Ly $\alpha$  luminosity for each LAE found in our survey using the following relation,

$$L(\text{Ly}\alpha) = 4\pi d_L^2 f(\text{Ly}\alpha) \quad \text{erg s}^{-1}, \quad (8)$$

where  $d_L$  is the luminosity distance, and  $f(\text{Ly}\alpha)$  is the Ly $\alpha$  flux estimated using  $D[IA]$  and  $IA$  magnitude below,

$$f(\text{Ly}\alpha) = \{f_\nu(IA) - f_\nu(D[IA])\}\Delta\nu \quad \text{erg s}^{-1} \text{ cm}^{-2}, \quad (9)$$

where  $f_\nu(IA) = 10^{-0.4(IA+48.6)} \text{ erg s}^{-1} \text{ cm}^{-2} \text{ Hz}^{-1}$ ,  $f_\nu(D[IA]) = 10^{-0.4(D[IA]+48.6)} \text{ erg s}^{-1} \text{ cm}^{-2} \text{ Hz}^{-1}$ , and  $\Delta\nu$  is the bandwidth in unit of Hz. In this calculation, we assume all the LAEs exist at the redshift shown in table 2 for each IA-band.

## 4. Discussion

### 4.1. Number Densities of Lyman $\alpha$ Emitters

Since we have found LAEs at  $z \simeq 3.3 - 4.8$ , we can investigate the number density evolution of LAEs as a function of redshift. The faintest  $\log L(\text{Ly}\alpha)$  is different for different IA band: 42.32 for IA527, 42.51 for IA574, 42.56 for IA598, 42.56 for IA624, 42.61 for IA651, 42.63 for IA679, and 42.67 for IA709, where  $L(\text{Ly}\alpha)$  is in units of  $\text{erg s}^{-1}$ . In order to compare with samples which is obtained by the same selection limit, we use the LAEs which is brighter than the IA limit,  $\log L(\text{Ly}\alpha) = 42.67$ . The number of LAEs brighter than  $\log L(\text{Ly}\alpha) = 42.67$  is 10 (IA527), 15 (IA574), 10 (IA598), 15 (IA624), 12 (IA651), 15 (IA679) and 15 (IA709), respectively, where  $L(\text{Ly}\alpha)$  is again in units of  $\text{erg s}^{-1}$ . Our effective survey area is 526 arcmin $^2$ . Then the volume covered by each filter is  $3.36 \times 10^5$  (IA527),  $3.63 \times 10^5$  (IA574),  $3.86 \times 10^5$  (IA598),  $3.85 \times 10^5$  (IA624),  $4.05 \times 10^5$  (IA651),  $4.12 \times 10^5$  (IA679), and  $3.78 \times 10^5$  (IA709) Mpc $^3$ , respectively. Therefore, we obtain the number density of LAEs for each filter as follows;  $n(\text{LAE}) \simeq 3.0 \times 10^{-5} \text{ Mpc}^{-1}$  at  $z \simeq 3.34$ ,  $4.1 \times 10^{-5} \text{ Mpc}^{-1}$  at  $z \simeq 3.72$ ,  $2.6 \times 10^{-5} \text{ Mpc}^{-1}$  at  $z \simeq 3.93$ ,  $3.9 \times 10^{-5} \text{ Mpc}^{-1}$  at  $z \simeq 4.12$ ,  $3.0 \times 10^{-5} \text{ Mpc}^{-1}$  at  $z \simeq 4.35$ ,  $3.6 \times 10^{-5} \text{ Mpc}^{-1}$  at  $z \simeq 4.58$ , and  $3.9 \times 10^{-5} \text{ Mpc}^{-1}$  at  $z \simeq 4.82$ . These results are shown in figure 9. Taking the estimated error into account, we may conclude that the LAE number density is constant at  $3.3 < z < 4.8$ .

Let us compare our results with published results. Fujita et al. (2003) obtained  $n(\text{LAE}) \simeq 6.4 \times 10^{-5}$  at  $z \simeq 3.7$ , being smaller by a factor of two than our value at  $z \simeq 3.7$ . This may be attributed to their survey is shallower than ours. Cowie & Hu (1998) made deep imaging survey for LAEs at  $z \sim 3.4$  in the Hubble Deep Field North and SSA22 and then found  $n(\text{LAE}) \sim 1 \times 10^{-3} \text{ Mpc}^{-1}$ . Kudritzki et al. (2000) obtained  $n(\text{LAE}) \sim 1 \times 10^{-3} \text{ Mpc}^{-1}$  for a blank field at  $z \simeq 3.1$ . Steidel et al. (2000) also obtained a large value for the SSA22a field;  $n(\text{LAE}) \sim 4 \times 10^{-3} \text{ Mpc}^{-1}$  at  $z \simeq 3.1$ . Although the field studied by Steidel et al. (2000) is a so-called

over density region, the LAE number density appear to depend on the survey depth. In this respect, since our LAE survey is a homogeneous one for LAEs between  $z \sim 3.3 - 4.8$ , the results shown in figure 9 can be used to investigate the evolution of LAE number density for the first time. Therefore, the constant number density of LAEs is one of important results in this study.

#### 4.2. Ly $\alpha$ Luminosity Distribution

In order to estimate contribution of LAEs to the cosmic star formation rate density at high redshift, we need a reliable Ly $\alpha$  luminosity function based on a large sample of LAEs. Since we have found 198 reliable candidates of LAEs at  $z \simeq 3.3 - 4.8$ , our sample is useful for this purpose.

In figure 10, we show the distribution of Ly $\alpha$  luminosities. We note that in this figure each bin width is  $\log L(\text{Ly}\alpha) = 0.2$  where  $L(\text{Ly}\alpha)$  is in units of  $\text{erg s}^{-1}$ . Our derived Ly $\alpha$  luminosities range from  $10^{42.3}$  to  $10^{43.2}$   $\text{erg s}^{-1}$ . These luminosities are higher than typical ones found in previous LAE surveys with use of a narrowband filter. The reason for this is that our IA filters have wider FWHMs than the narrowband filters used in the previous LAE surveys and thus our survey tend to find LAEs with a larger Ly $\alpha$  equivalent width. Therefore, we may underestimate the density at low luminosity range ( $\log L(\text{Ly}\alpha) < 42.5$ ) by the limit of  $L(\text{Ly}\alpha)$  at high-redshift. .

#### 4.3. UV Luminosity Distribution

Since the LAE candidates are selected by the estimation of photometric redshift, their UV magnitudes are bright enough to be detected on our  $R$  or  $i'$  image. Therefore, these candidates would be detected as LBG candidates. In this respect, our LAE candidates can be regarded as subsamples of LBGs. Therefore, it is interesting to compare UV luminosities of our LAEs with those of LBGs at similar redshifts. For this purpose, we estimate UV luminosities of our LAEs using broad band photometric data. We adopt  $R_c$ -band or  $i'$ -band as UV continuum;  $R$  for the LAEs found in *IA527*, *IA574*, and *IA598* catalogs, while  $i'$  for those in *IA624*, *IA651*, *IA679*, and *IA709* catalogs.

The results for LAEs of each IA catalog are shown in figure 11. In the lower-right panel of figure 11, we also show the results for all LAEs in our study. In this panel, we show the results of  $z \simeq 5.7$  LAE survey made by Hu et al. (2004) (filled squares).

Our results appear to be quite similar to their results although our redshift range ( $3.3 < z < 4.8$ ) is smaller than the redshift at the survey field of Hu et al. This suggests that the UV luminosity of LAEs does not show strong evolution from  $z \simeq 5.7$  to  $z \simeq 3.3$  although we need more data to confirm this.

Then we compare our results with those obtained for LBGs at  $z \sim 3 - 4$  (Steidel et al. 1999). As shown in figure 11, the number density of LBGs is systematically higher than that of LAEs in any UV luminosity (by a factor  $\sim 5$ ). This may in part explain why the SFRD derived from LAEs is significantly smaller than that derived from LBGs. This will be discussed later

(see Section 4.4.3).

#### 4.4. Star Formation Rate

##### 4.4.1. Star Formation Rate Based on Ly $\alpha$ Luminosity

We estimate the SFR for the emitters at each seven IA filters. We adopted the formula from Kennicutt (1998),

$$SFR = 7.9 \times 10^{-42} L(\text{H}\alpha) M_{\odot} \text{yr}^{-1} \quad (10)$$

where  $L(\text{H}\alpha)$  is in units of erg s $^{-1}$ , and from the case B recombination theory (Brocklehurst 1971),

$$L(\text{Ly}\alpha) = 8.7 L(\text{H}\alpha), \quad (11)$$

where  $L(\text{Ly}\alpha)$  is also in units of erg s $^{-1}$ , we can obtain the conversion relation between the SFR and the Ly $\alpha$  luminosity,

$$SFR(\text{Ly}\alpha) = 9.1 \times 10^{-43} L(\text{Ly}\alpha) M_{\odot} \text{yr}^{-1}. \quad (12)$$

Using this relation, we estimate the SFR for all LAEs. The results are given in figure 12. The obtained SFR ranges between  $1.8 M_{\odot} \text{yr}^{-1}$  and  $17.0 M_{\odot} \text{yr}^{-1}$  with a median SFR of  $4.1 M_{\odot} \text{yr}^{-1}$ . These results are consistent with previous surveys for high- $z$  LAEs (e.g., Cowie & Hu 1998; Keel et al. 1999; Kudritzki et al. 2000; Fujita et al. 2003; Ajiki et al. 2003; Cuby et al. 2003; Taniguchi et al. 2005).

##### 4.4.2. Star Formation Rate Based on UV Luminosity

We can also estimate SFR from rest-frame UV continuum and then we examine whether or not the SFR derived from the Ly $\alpha$  luminosity is consistent with that derived from the UV continuum luminosity for our sample. As described in section 4.3, we can estimate the rest-frame UV luminosity for all LAEs. Then we obtain the SFR based on UV luminosity using the following relation,

$$SFR(\text{UV}) = 1.4 \times 10^{-28} L_{\nu} M_{\odot}/\text{yr}, \quad (13)$$

where  $L_{\nu}$  is in units of erg s $^{-1}$  Hz $^{-1}$  (Kennicutt 1998).

The use of continuum magnitudes to estimate the SFR avoids the extremely complex problems of both the Ly $\alpha$  escape process and the uncertainties in the correction of the Ly $\alpha$  fluxes for intergalactic scattering which are present in the determination of the Ly $\alpha$  luminosity function.

##### 4.4.3. Comparison between $SFR(\text{Ly}\alpha)$ with $SFR(\text{UV})$

Now we compare  $SFR(\text{Ly}\alpha)$  with  $SFR(\text{UV})$ . The results are shown in figure 12 for LAEs found in each IA catalog. In the final panel of this figure, we also show results for all LAEs. We find that the two kinds of SFRs appears to be consistent within a factor of two for most of our LAEs, in particular for LAEs at redshift between  $z \simeq 3.3$  (IA527) and  $z \simeq 3.9$  (IA598).

However, for most LAEs at redshift between  $z \simeq 4.1$  and  $z \simeq 4.8$  (i.e.,  $z > 4$ ), there appears a tendency that  $SFR(\text{Ly}\alpha)$  is systematically smaller by a factor of  $\approx 1.3$  than  $SFR(\text{UV})$ . Such tendency is often found LAEs beyond  $z = 5$  (e.g., Hu et al. 2004; Ajiki et al. 2003; Taniguchi et al. 2005 and references therein). In order to see this tendency more clearly, we show the average  $SFR(\text{Ly}\alpha)/SFR(\text{UV})$  ratio,  $\langle \log SFR(\text{Ly}\alpha)/SFR(\text{UV}) \rangle$ , as a function of redshift in figure 13; the averages  $\log SFR(\text{Ly}\alpha)/SFR(\text{UV})$  are 0.03, 0.09, 0.92,  $-0.10$ ,  $-0.04$ ,  $-0.07$ , and  $-0.11$  for *IA527*, *IA574*, *IA598*, *IA624*, *IA651*, *IA679*, and *IA709*, respectively. Although these averages seem to slightly decrease with increasing redshift as shown in figure 13, it can be said that they are almost constant, i.e.,  $\langle \log SFR(\text{Ly}\alpha)/SFR(\text{UV}) \rangle \simeq 1$ . We summarize the observational properties of LAEs written above in table 4.

#### 4.4.4. Cosmic Evolution of the Star Formation Rate Density

The cosmic star formation history is one of the important key issues related to the formation and evolution of galaxies. In particular, the cosmic star formation history at high redshift has been mainly investigated by using galaxy samples based on the optical broad-band color selection; i.e., the Lyman break method (e.g., Madau et al. 1996; Steidel et al. 1999). More recently, LAEs have been also used to investigate the cosmic star formation history (e.g., Ajiki et al. 2003; Taniguchi et al. 2005; see for a review Taniguchi et al. 2003b). The use of LAE samples as well as LBG ones is important because such strong LAEs could contribute to the cosmic star formation rate significantly. However, the majority of them may be missed in broad-band photometric samples because they are often too faint to be contained in a broad-band magnitude-limited sample. One concern with surveys with a narrowband filter is that the redshift coverage is inevitably small. Therefore, information on the SFR is quite limited for a certain, discrete redshift. Since the LAEs found in this study are located from  $z \simeq 4.8$  to  $z \simeq 3.3$ , they allow us to investigate the cosmic star formation history viewed from LAEs systematically in the concerned redshift range. This is indeed one of main purposes of our IA filter survey.

We obtain the star formation rate density (SFRD) for each LAE sample at  $z \sim 3.3 - 4.8$ . The results are shown in the upper panel of figure 14 with previous results. Here, we use SFR calculated from  $\text{Ly}\alpha$  emission. The SFRDs shown in figure 14 are the simple sum of SFRs divided by the survey volume for all LAE candidates (open circles in the both panels) and LAE candidates of  $\log L(\text{Ly}\alpha) > 42.67$  (filled circles in the lower panel). The errors of the SFRD which arise from the photometric error is 8 % at most. Since we have not corrected for extinction for  $\text{Ly}\alpha$  emission and we have not made summing up by using a  $\text{Ly}\alpha$  luminosity function, these SFRDs are lower limit.

Our results show that SFRD for all LAE candidates basically decreases with increasing redshift. The decreasing trend may be caused from our selection limit. We compare the SFRD for LAEs with  $\log L(\text{Ly}\alpha) > 42.67$  (the filled circles in the lower panel of figure 14). The SFRD

derived for LAEs with  $\log L(\text{Ly}\alpha) > 42.67$  is nearly constant at  $z = 3.3\text{--}4.8$ . We can detect the LAE candidates from  $\log L(\text{Ly}\alpha) \simeq 42.4$  to  $\log L(\text{Ly}\alpha) \simeq 43.5$  (see figure 10). However since we observe only the bright-end of the number densities, we may miss a number of low-luminosity LAEs.

The data points with an upward arrow in figure 14 show the results of LAE searches. Since Ly $\alpha$  emission from high-redshift objects is absorbed either by the intergalactic medium or by the gas in the system itself or both, the blueward flux of Ly $\alpha$  emission should be underestimated. Therefore it could be desired that the SFRD using Ly $\alpha$  method must be corrected for this effect.

## 5. Summary

We have presented seven optical intermediate-band and multicolor observations of the Subaru / XMM-Newton Deep Field obtained with the Suprime-Cam on the 8.2 m Subaru telescope. The intermediate-band image covered a sky area of 526 arcmin $^2$  in the Subaru/XMM-Newton Deep Field (Ouchi et al. 2001). Our survey volume amounts to  $2.9 \times 10^6 \text{ Mpc}^3$  when we adopt a flat universe with  $\Omega_{\text{matter}} = 0.3$ ,  $\Omega_\Lambda = 0.7$ , and  $H_0 = 70 \text{ km s}^{-1} \text{ Mpc}^{-1}$ . We summarize the major conclusions of this study as follows:

- (1) In our survey we have found 409 *IA*-excess objects whose rest-frame Ly $\alpha$  emission-line equivalent widths are greater than 20 Å. Applying the photometric redshift technique, we obtain a sample of 198 Ly $\alpha$  emitter candidates.
- (2) From this LAE sample, we find that the number density of LAEs at  $z \sim 3.3 - 4.8$  is  $n(\text{LAE}) \sim 10^{-4} \text{ Mpc}^{-3}$  on average.
- (3) In order to investigate host galaxy properties of our LAEs, we investigate the rest-frame UV luminosity distributions of our LAE sample. The LAEs found in our study are fainter than those found for LAEs at  $z \simeq 5.7$  (Hu et al. 2004). We also find that the number density of LBGs is systematically higher by a factor of  $\approx 5$  than LAEs in any UV luminosity.
- (4) Using the observed Ly $\alpha$  luminosity, we estimate the SFR of our LAEs ranging from 1.8 to  $17.0 M_\odot \text{ yr}^{-1}$  with a median of  $4.1 M_\odot \text{ yr}^{-1}$ . We also estimate the SFR using the rest-frame UV luminosity. Comparing these two SFRs, we find that the average  $SFR(\text{Ly}\alpha)/SFR(\text{UV})$  ratios range from 0.5 to 2. This ratio is nearly constant between  $z \sim 3$  and 5.
- (5) Finally, we investigate the cosmic star formation history based on the star formation rate density (SFRD). We obtain  $SFRD \sim 10^{-3.6} M_\odot \text{ yr}^{-1} \text{ Mpc}^{-3}$  on average. Although we find a systematic decrease of  $SFRD$  with increasing redshift for all LAEs found in our survey, the SFRDs derived by using only bright LAEs ( $\log L(\text{Ly}\alpha) > 42.6$ ) appear to be nearly constant between  $z = 3.3$  and 4.8.

We would like to thank the Subaru Telescope staff and the SXDS team for their invaluable support.

able assistance. We would also like to thank K. Kodaira, S. Okamura, T. Yamada, K. Ohta, K. Shimasaku, and M. Ouchi for many useful suggestions, comments, and encouragement during the course of this study. We also thank T. Hayashino and H. Tamura for their kind technical help for construction of the IA filter system. This work was financially supported in part by the Ministry of Education, Culture, Sports, Science and Technology (Nos. 10044052, and 10304013) and JSPS (No. 15340059). MA, SSS, and TN are JSPS fellows. IRAF is distributed by the National Optical Astronomy Observatories, which are operated by the Association of Universities for Research in Astronomy, Inc., under cooperative agreement with the National Science Foundation.

## Appendix 1. Accuracy of our selection of LAEs using photometric redshifts

Since we select LAEs from IA-excess objects applying the photometric redshift method, it is important to examine if there is no significant selection effect as a function of redshift. In order to demonstrate it, we perform computer simulations in the following way. By comparing differences between the true (model) and estimated (photometric) redshifts, we can estimate the accuracy of our classification.

First, we make the simulated data from the galaxy SEDs taking account of the photometric errors. The galaxy SEDs are generated by using the population synthesis model, GALAXEV (Bruzual & Charlot 2003). To make various kinds of SEDs with strong emission line, we calculate the emission-line fluxes as a function of  $EW_0(\text{H}\alpha)$ ,  $EW_0([\text{OIII}])$ ,  $EW_0([\text{OII}])$ , and  $EW_0(\text{Ly}\alpha)$  instead of being proportional to the ionizing photon production rate. We adopt three cases of  $EW_0$  for each line:  $EW_0 = 100, 200,$  and  $400 \text{ \AA}$  for low- $z$  emission line galaxies,  $EW_0 = 65, 130,$  and  $260 \text{ \AA}$  for LAEs. Second, we select emission-line galaxies from simulated catalogs using the same criteria written in section 3.2. Third, we apply the photometric redshift method to the simulated data and compare the photometric redshift ( $z_{\text{phot}}$ ) with the model redshifts ( $z_{\text{model}}$ ).

Comparisons between  $z_{\text{model}}$  and  $z_{\text{phot}}$  are shown in figure 15. All the model LAEs are selected as LAEs using our photometric redshift method. Although some of the model low- $z$  emission line galaxies are selected as LAEs, the fraction of misclassification is less than 10 % for the all IA-filter bands. We, therefore, conclude that there is no significant selection effect as a function of redshift.

**Table 1.** The journal of observation

Band	$\lambda_c$ (Å)	$FWHM$ (Å)	Obs. Date	Total Integ. Time (s)	$M_{\text{lim}}(\text{AB})$ ( $3\sigma, 2''\phi$ )
<i>B</i>	4364	1008	2000 Nov 24,25 2002 Jan 13		
	Total			18000	28.2
<i>R<sub>c</sub></i>	6410	1576	2000 Aug 1 2000 Nov 21-24 2001 Nov 17 2002 Jan 13		
	Total			12000	27.4
<i>i'</i>	7589	1535	2000 Nov 25 2002 Jan 13		
	Total			13200	27.0
<i>z'</i>	9024	1409	2001 Oct 15,19,20	5700	25.8
<i>IA527</i>	5272	242	2002 Nov 6	5280	26.8
<i>IA574</i>	5743	271	2002 Nov 6	7200	26.5
<i>IA598</i>	6000	294	2002 Nov 6	6720	26.5
<i>IA624</i>	6226	299	2002 Oct 30,31	10560	26.7
<i>IA651</i>	6502	322	2002 Oct 30,31	9600	26.7
<i>IA679</i>	6788	336	2002 Oct 30,31	10560	26.8
<i>IA709</i>	7082	318	2002 Oct 30,31	11520	26.6

**Table 2.** The numbers of LAE ( $EW_{\text{rest}} > 20 \text{ \AA}$ ) candidates.

Filter	$z(\text{Ly}\alpha)$	$EW_{\text{obs}}$ ( $EW_{\text{rest}} = 20 \text{ \AA}$ )	$D[IA] - IA$ (mag)	IA-excess objects <sup>†</sup>	LAE candidates <sup>‡</sup>
IA527	3.336	86.711	0.332	74	64
IA574	3.723	94.457	0.325	47	40
IA598	3.934	98.684	0.314	42	20
IA624	4.120	102.401	0.320	48	26
IA651	4.347	106.941	0.311	60	16
IA679	4.582	111.645	0.311	77	17
IA709	4.824	116.480	0.339	61	15

<sup>†</sup> The number of IA-excess objects (see section 3.2).

<sup>‡</sup> The number of LAEs (see section 3.3).

**Table 3.** Catalog of LAE candidates

ID	$\Delta\text{RA}$ (arcmin)	$\Delta\text{DEC}$ (arcmin)	$B$	$R$	$i'$	$z'$	IA527	IA574	IA598	IA624	IA651	IA679	IA709
IA527													
7048	31.12	2.10	24.9	24.5	24.6	24.7	24.1	24.7	24.5	24.5	24.6	24.6	24.6
7988	17.98	2.26	27.6	26.8	27.1 > 26.2		25.5 > 26.9 > 26.9		27.0	26.7	27.0	26.6	
9442	4.69	2.65	26.0	25.3	25.3	25.3	25.0	25.4	25.4	25.5	25.4	25.4	25.4
9620	3.87	2.62	27.5	27.4 > 27.4 > 26.2			26.2 > 26.9 > 26.9 > 27.1		27.0 > 27.2 > 27.0				
11523	32.95	3.08	26.7	26.2	26.4 > 26.2		25.4	26.3	26.4	26.0	26.4	26.2	26.7
11538	29.70	3.08	27.2	26.6	26.5 > 26.2		25.5	26.5 > 26.9	27.0	26.8 > 27.2	26.8		
13069	15.33	3.46	26.8	26.1	26.3 > 26.2		25.5	26.2	26.3	26.1	26.1	26.3	26.2
15427	14.95	3.99	28.4 > 27.8 > 27.4 > 26.2				26.1 > 26.9 > 26.9 > 27.1 > 27.1 > 27.2 > 27.0						
15823	13.32	4.09	27.1	26.7	27.0 > 26.2		25.8	26.2	26.4	27.0	26.8	26.7	26.6
17533	7.25	4.47	27.1	26.5	26.3 > 26.2		25.6	26.8	26.5	26.2	26.9	26.9	26.7
19286	16.25	4.90	27.4	26.8	26.6 > 26.2		25.7	26.7	26.3 > 27.1	27.0 > 27.2	26.6		
27691	3.68	6.87 > 28.6 > 27.8 > 27.4 > 26.2					25.8 > 26.9 > 26.9 > 27.1 > 27.1 > 27.2 > 27.0						
28584	32.53	7.12	26.1	25.8	25.9	25.9	25.3	25.8	26.0	25.8	25.6	26.0	25.8
28996	32.98	7.22	26.1	25.7	25.7	25.3	24.9	25.8	25.9	25.6	25.5	25.8	25.6
29083	17.27	7.19	27.7	26.7	26.6 > 26.2		25.9 > 26.9	26.8	26.6	26.6	26.9	26.7	
37812	13.88	9.34	26.8	25.9	25.8	25.6	25.3	26.5	25.8	25.6	25.7	26.0	25.9
38785	23.54	9.45	26.6	26.0	26.0 > 26.2		25.4	26.5	26.1	26.8	26.3	26.3	26.1
41668	27.31	10.14	27.6	26.8	26.9 > 26.2		25.8 > 26.9	26.8 > 27.1 > 27.1		27.0 > 27.0			
44636	10.55	10.97	26.3	25.9	25.7	26.0	25.4	25.7	26.4	26.0	26.4	25.9	26.0
47969	28.10	11.70	26.3	25.5	25.4	25.3	24.3	25.5	25.5	25.9	25.3	25.6	25.5
49443	5.92	12.04 > 28.6	27.1	27.1 > 26.2			26.0 > 26.9 > 26.9 > 27.1	26.5 > 27.2 > 27.0					
51844	27.84	12.52	27.6	26.9	27.1 > 26.2		25.6 > 26.9 > 26.9 > 27.1 > 27.1 > 27.2	26.6					
54027	8.21	13.04	27.0	25.8	25.6	25.5	25.2	26.1	25.7	25.7	25.7	25.6	25.7
55020	22.84	13.23	27.9	27.3	27.4 > 26.2		26.0 > 26.9 > 26.9 > 27.1 > 27.1 > 27.2 > 27.0						
55100	25.17	13.25	26.9	26.7	26.5	26.1	25.8	26.3 > 26.9	26.9 > 27.1 > 27.2	26.9			
55848	20.90	13.43	27.1	26.4	26.3 > 26.2		24.7	26.1 > 26.9	26.9	26.4	26.6	26.9	
57223	13.32	13.75	28.5	27.4 > 27.4 > 26.2			26.0 > 26.9 > 26.9 > 27.1 > 27.1 > 27.2 > 27.0						
57844	30.39	13.89	27.0	26.0	26.2 > 26.2		25.4 > 26.9	26.6	26.3	26.1	26.3	26.7	
59074	24.21	14.14 > 28.6	27.6 > 27.4 > 26.2				26.2 > 26.9 > 26.9 > 27.1 > 27.1 > 27.2 > 27.0						
59405	24.81	14.24	25.7	25.4	25.4	25.7	24.7	25.4	25.3	25.5	25.3	25.5	25.4
60224	12.82	14.45	27.1	26.4	26.5 > 26.2		25.5	26.4 > 26.9	26.2	26.6	26.5	26.5	
60455	16.47	14.52	26.4	25.7	25.6	25.9	25.2	25.7	25.9	25.6	25.6	25.8	25.8
60664	12.93	14.52	27.4	26.7	26.9 > 26.2		25.9	26.8 > 26.9	26.9	26.1	27.1 > 27.0		

**Table 3.** (Continued.)

ID	$\Delta\text{RA}$ (arcmin)	$\Delta\text{DEC}$ (arcmin)	<i>B</i>	<i>R</i>	<i>i'</i>	<i>z'</i>	IA527	IA574	IA598	IA624	IA651	IA679	IA709
63293	13.47	15.21	27.3	26.5	26.4 > 26.2	25.8	26.8	26.4	26.4	26.5	26.3	26.5	
69085	10.84	16.51	27.5	27.4	27.0 > 26.2	26.2 > 26.9	26.7 > 27.1	26.7	26.8 > 27.0				
70551	27.75	16.89	26.7	26.0	26.0	25.7	25.2	25.9	25.9	26.1	25.8	25.9	26.0
71679	23.43	17.15	26.7	25.9	25.9	25.7	25.0	26.2	26.0	25.6	25.9	25.8	25.9
72094	15.20	17.23	26.5	25.8	25.8	25.8	25.4	26.1	25.9	25.8	26.0	25.9	25.8
72647	9.68	17.36	27.4	26.9	27.1 > 26.2	25.6	26.4 > 26.9	26.7	26.6 > 27.2	26.7			
74055	19.68	17.67	27.8	27.4	27.3 > 26.2	25.9 > 26.9 > 26.9 > 27.1 > 27.1	27.0 > 27.0						
74299	9.17	17.72	27.6	27.6	26.5 > 26.2	26.1 > 26.9 > 26.9	26.6 > 27.1 > 27.2 > 27.0						
75353	18.23	17.99	27.6	26.9	27.1 > 26.2	25.7 > 26.9	26.8 > 27.1	26.9	27.2 > 27.0				
77460	23.33	18.48	27.0	26.1	26.0	26.0	25.4	25.9	26.4	26.0	26.1	26.1	26.1
78162	9.64	18.67	25.6	24.8	24.8	25.1	24.3	24.9	24.9	24.8	24.8	24.8	24.8
80388	13.88	19.15	27.9	27.4 > 27.4	26.2	26.0 > 26.9 > 26.9	26.6 > 27.1 > 27.2	26.8					
81380	33.07	19.44	26.8	25.8	25.6	25.9	25.3	26.0	25.9	25.8	25.6	25.8	25.6
82145	2.78	19.63	27.6	26.6	27.1 > 26.2	25.8	26.7	26.8	26.6 > 27.1 > 27.2 > 27.0				
82756	22.50	19.73	27.6	27.0	27.3 > 26.2	25.5 > 26.9 > 26.9 > 27.1 > 27.1	27.0 > 27.0	26.6					
83157	25.82	19.86	26.5	25.5	25.6	25.8	24.5	25.9	26.0	25.7	25.4	25.6	25.4
86220	11.33	20.53	27.2	26.5	26.5 > 26.2	25.8	26.4	26.7	26.4	26.7 > 27.2 > 27.0			
87141	4.41	20.77	26.7	25.8	25.6	25.4	24.9	26.0	25.9	26.1	25.7	26.0	25.8
87553	11.80	20.85	27.1	26.4	26.7 > 26.2	25.2 > 26.9 > 26.9	26.1	26.5	26.2	26.7			
88785	30.56	21.13	27.2	26.1	26.1	26.1	25.5	26.0	26.1	26.2	26.1	26.4	26.1
89485	24.51	21.30	27.0	26.2	26.2 > 26.2	25.5	26.3	26.1	26.1	26.2	26.4	26.0	
89896	2.73	21.38 > 28.6 > 27.8 > 27.4 > 26.2				26.1 > 26.9 > 26.9 > 27.1	27.0 > 27.2 > 27.0						
90874	28.10	21.69	26.8	26.4	26.3 > 26.2	25.4 > 26.9	26.3	26.6	26.2	26.6	26.3		
94639	10.37	22.51	28.0	27.4	27.2 > 26.2	25.8 > 26.9 > 26.9 > 27.1 > 27.1 > 27.2 > 27.0							
94941	9.14	22.58	28.4 > 27.8 > 27.4 > 26.2			26.1 > 26.9 > 26.9 > 27.1 > 27.1 > 27.2 > 27.0							
95272	30.36	22.69 > 28.6	27.6 > 27.4 > 26.2			26.1 > 26.9 > 26.9 > 27.1 > 27.1 > 27.2 > 27.0							
96625	12.26	22.98	26.5	26.2	26.2 > 26.2	25.5 > 26.6	26.3	26.1	26.4	26.4	26.1		
99496	33.17	23.64	27.4	27.2 > 27.4 > 26.2		25.7 > 26.9 > 26.9	26.7 > 27.1 > 27.2	26.7					
100145	24.45	23.81	27.5	26.7	26.8 > 26.2	25.6 > 26.9	26.7 > 27.1	26.4	27.1	26.6			
101147	3.67	24.04	27.8	27.0	26.4	25.8	26.0 > 26.9 > 26.9 > 27.1 > 27.1	26.9 > 27.0					
102766	10.22	24.38	27.2	26.7	26.7 > 26.2	25.7 > 26.9	26.4 > 27.1 > 27.1 > 27.2	26.7					
IA574													
6580	23.34	2.02	26.8	25.3	25.4	25.1	26.1	24.9	26.2	25.4	25.5	25.5	25.4
10969	9.65	3.06	27.0	25.4	25.5	25.8	26.0	24.5	25.4	25.6	25.6	25.4	25.4
11379	3.01	3.15	28.5	26.7	26.4 > 26.2 > 27.2	25.7	26.7 > 27.1	26.9	27.1 > 27.0				

**Table 3.** (Continued.)

ID	$\Delta\text{RA}$ (arcmin)	$\Delta\text{DEC}$ (arcmin)	$B$	$R$	$i'$	$z'$	IA527	IA574	IA598	IA624	IA651	IA679	IA709	
13034	31.65	3.51	28.4	27.5 > 27.4 > 26.2 > 27.2			26.0 > 26.9		26.9 > 27.1 > 27.2 > 27.0					
21251	14.75	5.62 > 28.6	27.5	27.3 > 26.2 > 27.2			25.9 > 26.9 > 27.1 > 27.1 > 27.2						26.9	
22223	11.00	5.85	27.5	26.5	26.4 > 26.2	26.7	25.6 > 26.9	26.3	26.5	26.8	26.3			
25092	16.05	6.57	27.9	26.5	26.7 > 26.2 > 27.2	25.7	26.4	26.5	26.8	26.8	26.5			
34695	19.17	9.03	27.2	25.7	25.5	25.8	26.6	24.7	25.7	25.8	25.7	25.7	25.7	
36987	15.02	9.52 > 28.6	27.3	27.1 > 26.2 > 27.2			25.8	26.6	26.4 > 27.1		27.1 > 27.0			
45242	28.40	11.64	27.9	26.6	26.5 > 26.2	26.7	25.7 > 26.9	26.8	26.5	26.7 > 27.0				
46603	32.09	11.96	27.7	26.3	25.7	25.5 > 27.2	24.4	26.7	26.4	26.4	26.0	25.7		
51420	28.60	13.02	27.6	25.9	26.0	25.5	26.7	25.2	25.8	25.9	25.8	26.1	25.9	
53464	29.48	13.53	27.2	25.7	25.8	26.1	26.6	25.0	25.6	25.8	25.7	25.7	25.7	
53930	3.36	13.66	27.5	25.5	25.6 > 26.2	26.4	24.8	25.1	25.6	25.5	25.8	25.8		
54185	18.45	13.68	28.2	26.4	26.4 > 26.2 > 27.2	25.6	26.0	26.5	26.4	26.6	26.3			
55740	5.22	14.04	28.5	26.4	26.3	26.0 > 27.2	25.6	25.4	26.7	26.5	26.8	26.7		
55786	21.14	14.03	27.6	26.3	26.1 > 26.2	26.6	25.5	26.0 > 27.1	26.9	26.3	26.5			
57174	11.44	14.36 > 28.6	26.9	27.0 > 26.2 > 27.2			25.8 > 26.9 > 27.1		26.8 > 27.2 > 27.0					
58770	31.72	14.78	27.7	26.1	25.9 > 26.2	26.3	25.3	26.3	25.9	26.4	26.3	26.2		
65463	27.52	16.41	27.1	25.8	25.7	25.6	26.9	25.2	25.8	25.7	25.7	25.6	25.8	
65839	15.68	16.47	27.5	25.7	25.9	25.8	26.8	25.2	25.0	25.7	25.9	25.9	25.8	
66933	17.41	16.71	27.8	26.7	26.5	26.1	27.1	25.8	26.1	26.5	26.5	26.5	26.8	
68446	22.09	17.10	28.1	26.2	26.3 > 26.2 > 27.2	25.5	26.5	26.4	26.1	26.3	26.3	26.3		
69065	26.74	17.21 > 28.6	27.8	27.3 > 26.2 > 27.2			26.0 > 26.9	26.8	27.0 > 27.2 > 27.0					
71041	20.31	17.71	26.8	25.4	25.2	25.2	26.2	24.7	25.4	25.5	25.3	25.3	25.4	
72707	26.20	18.09	28.4	27.7 > 27.4 > 26.2 > 27.2			26.0 > 26.9 > 27.1 > 27.1 > 27.2 > 27.0							
73613	8.82	18.37	26.9	25.4	25.5	25.7	26.4	24.5	25.5	25.4	25.4	25.5	25.6	
74326	8.84	18.54	27.1	25.6	25.6	26.1	26.2	25.2	25.8	25.8	25.7	25.9	25.6	
75127	21.00	18.69	26.7	25.5	25.5	25.9	26.5	24.9	25.5	25.5	25.5	25.7	25.5	
75930	25.58	18.89	28.2	27.1	27.1 > 26.2 > 27.2		25.5 > 26.9 > 27.1		26.5	26.9 > 27.0				
76201	11.48	18.96	27.3	25.9	25.9 > 26.2	26.2	25.0	26.0	25.8	25.9	26.1	25.8		
77116	28.22	19.32	27.5	26.2	26.2 > 26.2 > 27.2	25.4	26.4	26.2	26.0	26.3	26.7			
78959	28.68	19.65	28.3	27.0	26.8 > 26.2 > 27.2		25.2 > 26.9	27.0	26.8 > 27.2		26.8			
79754	3.03	19.82 > 28.6 > 27.8 > 27.4 > 26.2 > 27.2					25.9 > 26.9 > 27.1 > 27.1 > 27.2 > 27.0							
82975	4.29	20.60	28.5 > 27.8 > 27.4 > 26.2 > 27.2				26.0 > 26.9	26.8	26.6 > 27.2 > 27.0					
85436	24.16	21.39	28.1	27.4	27.0 > 26.2 > 27.2		25.9 > 26.9 > 27.1 > 27.1		27.1 > 27.2					
90651	22.42	22.51 > 28.6 > 27.8 > 27.4 > 26.2					27.0 > 26.9 > 27.1 > 27.1 > 27.2		26.7					
91865	9.85	22.81	27.4	25.7	25.5	25.3	27.1	25.0	25.7	25.7	25.8	25.5		

**Table 3.** (Continued.)

ID	$\Delta\text{RA}$ (arcmin)	$\Delta\text{DEC}$ (arcmin)	$B$	$R$	$i'$	$z'$	IA527	IA574	IA598	IA624	IA651	IA679	IA709
96523	32.25	23.86 > 28.6	26.6	26.7 > 26.2 > 27.2	25.6	26.2 > 27.1	26.3	27.0 > 27.0					
99338	14.02	24.48 28.4	27.1	27.2 > 26.2 > 27.2	25.8	26.9 > 27.1	26.5	27.0 > 27.0					
IA598													
10519	8.44	2.93 27.4	25.9	26.0 > 26.2	26.4	26.0	25.2	26.2	25.9	25.9	26.5		
12390	15.71	3.39 27.6	25.3	25.5 25.4	26.7	26.3	24.9	25.3	25.5	25.4	25.5		
13299	7.22	3.65 28.0	25.7	26.0 > 26.2	26.5	25.9	25.1	25.9	25.9	26.0	25.8		
27435	21.87	7.15 28.3	26.6	26.4 > 26.2 > 27.2	26.5	25.4 > 27.1	26.7	26.7	26.8				
33977	23.33	8.70 28.2	26.3	26.4 25.7 > 27.2	25.7	25.6	26.4	26.5 > 27.2	26.2				
37912	16.71	9.77 27.5	25.6	25.7 25.6	26.4	25.7	25.1	25.8	25.7	25.6	25.8		
53728	33.03	13.66 28.2	26.3	26.4 25.8	27.1 > 26.9	25.5	26.9	26.8	26.3	26.3			
53761	3.36	13.66 27.5	25.5	25.6 > 26.2	26.4	24.8	25.0	25.6	25.6	25.8	25.8		
55275	5.22	14.04 28.4	26.3	26.3 26.0 > 27.2	25.6	25.4	26.6	26.4	26.8	26.7			
58192	18.42	14.76 28.0	25.6	25.7 25.9	26.1	26.2	25.1	25.7	25.7	26.0	26.1		
59826	15.24	15.13 28.4	28.4	27.7 > 27.4 > 26.2 > 27.2 > 26.9	26.0 > 27.1 > 27.1 > 27.2 > 27.0								
60845	31.10	15.46 27.4	25.5	25.7 25.9	26.5	26.7	25.1	25.0	25.7	25.9	25.9		
64675	15.68	16.46 27.6	25.8	26.1 25.9	26.7	25.3	25.0	25.8	25.9	25.9	25.9		
65983	8.87	16.79 > 28.6	26.4	26.9 > 26.2	27.1 > 26.9	25.5	26.7	26.6	27.1	26.8			
80344	22.09	20.48 > 28.6	26.7	27.0 > 26.2 > 27.2 > 26.9	25.5	26.9	27.1	26.8 > 27.0					
81987	22.99	20.98 27.5	26.2	26.3 > 26.2 > 27.2	26.5	25.5	26.4	26.2	26.6	26.1			
85081	27.30	21.70 27.6	26.5	26.3 25.8 > 27.2	25.8	25.6 > 27.1	26.4	26.5	26.3				
87226	9.98	22.25 28.2	26.0	26.1 > 26.2 > 27.2 > 26.9	25.2	26.6	26.4	26.6	26.1				
89279	11.33	22.83 27.6	24.7	24.3 24.4	26.3	25.5	24.1	25.1	25.0	24.8	24.8		
92776	32.35	23.61 28.5	27.1 > 27.4 > 26.2 > 27.2	26.4	25.9 > 27.1 > 27.1 > 27.2	26.7							
IA651													
18239	3.23	4.91 > 28.6	26.3	26.5 > 26.2 > 27.2 > 26.9 > 26.9 > 27.1	25.3	26.8	26.4						
18481	2.62	5.00 > 28.6	26.2	26.5 > 26.2 > 27.2 > 26.9 > 26.9 > 27.1	25.4	26.7	27.0						
18929	33.00	5.10 > 28.6	25.7	25.8 25.5 > 27.2 > 26.9 > 26.9 > 25.3	25.3	25.9	26.4						
56248	15.97	14.13 > 28.6	25.5	25.7 25.7 > 27.2 > 26.9	26.3	25.5	25.1	25.7	25.8				
58954	31.80	14.78 > 28.6	25.4	25.6 > 26.2 26.5	26.2	26.6	25.8	24.7	25.5	25.4			
60304	18.15	15.06 > 28.6	25.9	26.0 > 26.2 > 27.2	26.8	26.6	25.5	25.4	25.9	26.1			
61944	27.74	15.45 28.3	26.7	27.1 > 26.2 > 27.2 > 26.9 > 26.9	26.3	25.9	27.2	27.0					
62565	19.97	15.59 > 28.6	26.1	26.2 > 26.2 > 27.2	26.8	26.8	26.3	25.4	26.1	26.2			
65736	19.27	16.40 > 28.6	26.6	26.7 > 26.2 > 27.2 > 26.9 > 26.9 > 27.1	25.8	26.9	26.5						
68104	22.64	16.91 > 28.6	26.2	26.5 > 26.2 > 27.2 > 26.9 > 26.9 > 27.1	25.6	26.3	26.6						

**Table 3.** (Continued.)

ID	$\Delta\text{RA}$ (arcmin)	$\Delta\text{DEC}$ (arcmin)	$B$	$R$	$i'$	$z'$	IA527	IA574	IA598	IA624	IA651	IA679	IA709
70056	4.12	17.39	28.4	26.0	26.1	25.5 > 27.2 > 26.9 > 26.9 > 27.1	25.4	26.3	26.7				
87781	9.50	21.64	28.4	25.7	25.7	25.7 > 27.0 > 26.6 > 26.9 > 27.1	25.2	25.7	25.8				
95072	33.02	23.39 > 28.6	26.8	27.3 > 26.2 > 27.2 > 26.9 > 26.9 > 27.1			25.5 > 27.2 > 27.0						
96758	9.34	23.84 > 28.6	26.2	26.1	26.0	26.6 > 26.9 > 26.9 > 27.1	25.3	26.7	26.0				
97673	30.68	24.03	28.2	26.1	26.2 > 26.2 > 27.2 > 26.9 > 26.9 > 27.1		25.4	25.7	26.5				
98943	14.27	24.33 > 28.6	25.6	25.6 > 26.2 > 27.2		26.5 > 26.4 > 26.7	25.2	25.4	25.7				
IA679													
9065	11.03	3.02 > 28.6	26.8	26.7 > 26.2 > 27.2 > 26.9 > 26.9 > 27.1 > 27.1			25.8	26.6					
11843	12.88	3.78 > 28.6	25.1	24.8	24.6	26.3 > 25.6 > 26.3 > 26.0	25.0	24.1	25.1				
16415	12.58	5.04 > 28.6	26.1	26.3 > 26.2 > 27.2 > 26.9 > 26.9 > 27.1 > 27.1			25.3	26.5					
18878	19.37	5.73 > 28.6	26.9	26.9 > 26.2 > 27.2 > 26.9 > 26.9 > 27.1			26.7	25.8 > 27.0					
19202	16.85	5.83 > 28.6	26.7	26.7 > 26.2 > 27.2 > 26.9 > 26.9 > 27.1 > 27.1			25.6	26.7					
24769	18.54	7.37 > 28.6	25.5	25.6	25.5 > 27.2 > 26.9	26.4 > 27.1	26.9	24.7	25.7				
33768	2.80	9.83 > 28.6	26.1	25.9	26.1 > 27.2 > 26.9 > 26.9 > 27.1		26.6	25.4	25.8				
46786	11.24	13.33 > 28.6	26.3	26.0 > 26.2 > 27.2 > 26.9 > 26.9 > 27.1 > 27.1			25.4	25.9					
47730	19.04	13.55 > 28.6	26.2	25.8	25.7 > 27.2 > 26.9 > 26.9 > 26.9 > 27.1		25.3	25.5					
52102	18.29	14.62 > 28.6	26.2	26.3	26.1 > 27.2	26.7 > 26.8	27.0	26.0	25.4	25.8			
57794	18.81	16.05	28.4	26.6	26.8 > 26.2 > 27.2 > 26.9 > 26.9 > 27.1 > 27.1		25.7	26.7					
60173	24.90	16.68 > 28.6	25.9	25.6	25.7 > 27.2	26.7 > 26.9 > 27.1	26.8	25.0	26.1				
62116	18.75	17.17 > 28.6	26.1	25.9	26.1 > 27.2	26.9 > 26.6 > 27.1 > 27.1		25.1	26.1				
64479	13.46	17.75 > 28.6	26.3	26.2	25.7 > 27.2	26.9 > 26.6 > 26.3	26.4	25.5	26.0				
65576	13.78	18.07 > 28.6	25.6	25.2	25.2 > 27.2	26.6 > 26.2	26.3	26.4	24.8	25.2			
74655	23.99	20.40 > 28.6	27.2	27.0 > 26.2 > 27.2		26.9 > 26.9 > 27.1 > 27.1		25.9	26.6				
89098	32.65	24.33 > 28.6	26.2	26.4	26.2	26.8 > 26.9 > 26.9 > 27.1 > 27.1		25.4	26.2				
IA709													
8190	6.33	2.65 > 28.6	26.0	25.5	26.0 > 27.2	26.5 > 26.9 > 27.1	26.2	25.9	25.1				
13683	3.29	4.01 > 28.6 > 27.8		27.3 > 26.2 > 27.2 > 26.9 > 26.9 > 27.1 > 27.1 > 27.2			25.8						
18701	13.61	5.25 > 28.6	27.2	26.2 > 26.2 > 27.2 > 26.9 > 26.9 > 27.1 > 27.1 > 27.2			25.5						
31658	3.29	8.35 > 28.6	27.2	26.0 > 26.2 > 27.2 > 26.9 > 26.9 > 27.1 > 27.1 > 27.2			25.3						
33815	21.05	8.91 > 28.6	26.2	25.4	25.3 > 27.2 > 26.9 > 26.9	26.8 > 27.1 > 27.2		24.9					
34592	22.59	9.08 > 28.6	26.7	26.0 > 26.2 > 27.2 > 26.9 > 26.9 > 27.1 > 27.1 > 27.2			25.3						
38261	20.65	9.95 > 28.6	26.8	26.2	26.0 > 27.2 > 26.9 > 26.9	27.0 > 27.1 > 27.2		25.5					
51167	3.36	13.00 > 28.6	26.9	25.8	25.8 > 27.2 > 26.9 > 26.6	27.1 > 27.1 > 27.2		25.2					
55557	13.08	14.03 > 28.6	26.0	25.5	26.1 > 27.2 > 26.9 > 26.9	27.1 > 27.1 > 27.1		25.6	25.0				

**Table 3.** (Continued.)

ID	$\Delta\text{RA}$ (arcmin)	$\Delta\text{DEC}$ (arcmin)	$B$	$R$	$i'$	$z'$	IA527	IA574	IA598	IA624	IA651	IA679	IA709
59617	4.65	14.98 > 28.6	25.9	25.4	25.8 > 27.2 > 26.9 > 26.9 > 27.1 > 27.1 > 27.2								24.4
66451	9.95	16.61 > 28.6	26.5	25.7	25.9 > 27.2 > 26.9 > 26.9 > 27.1 > 27.1 > 27.2								25.2
72647	25.39	18.09 > 28.6	27.0	27.3 > 26.2 > 27.2 > 26.9 > 26.9 > 27.1 > 27.1									25.8
80850	29.77	20.09 > 28.6	26.6	26.2 > 26.2 > 27.2 > 26.9 > 26.9 > 27.1 > 27.1 > 27.2									25.5
83599	32.00	20.73 > 28.6	27.2	27.2 > 26.2 > 27.2 > 26.9 > 26.9 > 27.1 > 27.1 > 27.2									25.7
84928	11.99	21.07 > 28.6	26.8	26.6 > 26.2 > 27.2 > 26.9 > 26.9 > 27.1 > 27.1 > 27.2									25.2

## References

- Ajiki, M., et al. 2002, ApJ, 576, L25
- Ajiki, M., et al. 2003, AJ, 126, 2091
- Ajiki, M., et al. 2004, PASJ, 56, 597
- Barger, A. J., et al. 2001, AJ, 122, 2177
- Becker, R. H., et al. 2001, AJ, 122, 2850
- Beckwith, S. V. W. et al. 2003, BAAS, 202, 1705
- Bell, E. F., et al. 2004, ApJ, 608, 752
- Bertin, E., & Arnouts, A. 1996, A&AS, 117, 393
- Brocklehurst, M. 1971, MNRAS, 153, 471
- Bruzual, A. G., & Charlot, S. 2003, MNRAS, 344, 1000
- Bunker, A. J., Stanway, E. R., Ellis, R. S., McMahon, R. G. 2004, MNRAS, 355, 374
- Calzetti, D., Armus, L., Bohlin, R. C., Kinney, A. L., Koornneef, J., & Storchi-Bergmann, T. 2000, ApJ, 533, 2
- Cohen, J. G., Hogg, D. W., Blandford, R., Cowie, L. L., Hu, E., Songalia, A., Shopbell, P., & Richberg, K. 2000, ApJ, 545, 32
- Coleman, G. D., Wu, C.-C., & Weedman, D. W. 1980, ApJS, 43, 393
- Connolly, A. J., Szalay, A. S., Dickinson, M., Subbarao, M. U., & Brunner, R. J. 1997, ApJ, 486, 11
- Cowie, L. L., Songalia, A., Hu, E. M., & Cohen, J. G. 1996, AJ, 112, 839
- Cowie, L. L., & Hu, E. M. 1998, AJ, 115, 1319
- Cuby, J.-G., Le Fevre, O., McCracken, H., Cuillandre, J. C., Magnier, E., Meneux, B. 2003, A&A, 405, 19
- Dawson, S., Stern, D., Bunker, A. J., Spinrad, H., & Dey, A. 2001, AJ, 122, 598
- Dey, A., Spinrad, H., Stern, D., Graham, J. R., & Chaffee, F. H. 1998, ApJ, 498, L93
- Fan, X., Strauss, M. A., Schneider, D. P., Becker, R. H., White, R. L., Narayanan, V. K., Richards, G. T., Pentericci, L., et al. 2002, AAS, 20111414
- Fioc, M., & Rocca-Volmerange, B. 1997, A&A, 326, 950
- Fujita, S. S., et al. 2003, AJ, 125, 13
- Giavalisco, M., Dickinson, M., Ferguson, H. C., Ravindranath, C., Kretchmer, C., Moustakas, L. A., Madau, P., Fall, S. M., et al. 2004, ApJ, 600, L103
- Haiman, Z. & Spaans, M. 1999, ApJ, 518, 138
- Hayashino, T., et al. 2000, SPIE, 4008, 397
- Hayashino, T., et al. 2003, PNAOJ, 7, 33
- Hu, E. M., McMahon, R. G., Egami, E. 1996, ApJ, 459, L53
- Hu, E. M., Cowie, L. L., McMahon, R. G., Capak, P., Iwamuro, F., Kneib, J. -P., Maihara, T., & Motohara, K. 2002, ApJ, 568, L75
- Hu, E. M., Cowie, L. L., Capak, P., McMahon, R. G., Hayashino, T., & Komiyama, Y. 2004, AJ, 127, 563
- Iwata, I., Ohta, K., Tamura, N., Ando, M., Wada, S., Watanabe, C., Akiyama, M., & Aoki, K. 2003, PASJ, 55, 415
- Iye, M., et al. 2004, PASJ, 56, 381

- Kaifu, N., et al. 2000, PASJ, 52, 1
- Kajisawa, M., Yamada, T. 2001, PASJ, 53, 833
- Kajisawa, M., et al. 2000, PASJ, 52, 53
- Kauffmann, G., Haehnelt, M. 2000, MNRAS, 311, 576
- Keel, W. C., Cohen, S. H., Windhorst, R. A., & Waddington, I. 1999, AJ, 118, 2547
- Kennicutt, R. 1998, ARA&A, 36, 189
- Kodaira, K., et al. 2003, PASJ, 55, L17
- Kudritzki, R. -P., et al. 2000, ApJ, 536, 19
- Kurk, J. D., Cimatti, A., di Serego Alighieri, S., Vernet, J., Daddi, E., Ferrara, A., & Ciardi, B. 2004, A&A, 422, L13
- Landolt, A. U. 1992, AJ, 104, 340
- Lanzetta, K. M., Yahil, A., & Fernández-Soto, A. 1996, Nature, 381, 759
- Leitherer, C. & Heckman, T. M. 1995, ApJS, 96, 9
- Lilly, S. J., LeFèvre, O., Hammer, F., & Crampton, D. 1996, ApJ, 460, L1
- Loeb, A., & Barkana, R. 2001, ARA&A, 39, 19
- Lowenthal, J. D., Koo, D. C., Guzman, R., Gallego, J., Phillips, A. C., Faber, S. M., Vogt, N. P., Illingworth, G. D., & Gronwall, C. 1997, ApJ, 481, 637
- Madau, P., Ferguson, H. C., Dickinson, M. E., Giavalisco, M., Steidel, C. C., & Fruchter, A. 1996, MNRAS, 283, 1388
- Martin, C. L. & Sawicki, M. 2004, ApJ, 603, 414
- Miyazaki et al. 2002, PASJ, 54, 833
- Oke, J. B. 1974, ApJS, 27, 21
- Oke, J. B. 1990, AJ, 99, 1621
- Osterbrock, D. E. 1989, *Astrophysics of Gaseous Nebulae and Active Galactic Nuclei*. University Science Books, Sausalito, CA
- Ouchi, M., et al. 2001, ApJ, 558, L83
- Ouchi, M., Shimasaku, K., Okamura, S., Furusawa, H., Kashikawa, N., Ota, K., Doi, M., Hamabe, M., et al. 2004, ApJ, 611, 660
- Partridge, R. B., & Peebles, P. J. E. 1967, ApJ, 147, 868
- Pettini, M., Shapley, A. E., Steidel, C. C., Cuby, J. -G., Dickinson, M., Moorwood, A. F. M., Adelberger, K. L., & Giavalisco, M. 2001, ApJ, 554, 981
- Pirzkal, N., et al. 2004, ApJS, 154, 501
- Pritchett, C. J. 1994, PASP, 106, 1052
- Rhoads, J. E., Malhotra, S., Dey, A., Stern, D., Spinrad, H., Jannuzzi, B. T. 2000, ApJ, 545, L85
- Rhoads, J. E., Dey, A., Malhotra, S., Stern, D., Spinrad, H., Jannuzzi, B. T., Dawson, S., Brown, M. J. I., & Landes, E. 2003, AJ, 125, 1006
- Santos, M. R., Ellis, R. S., Kneib, J. -P., Richard, J., & Kuijken, K. 2004, ApJ, 606, 683
- Shapley, A. E., Steidel, C., Adelberger, K. L., Dickinson, M., Giavalisco, M., & Pettini, M. 2001, ApJ, 562, 95
- Shapley, A. E., Steidel, C. C., Pettini, M., & Adelberger, K. L. 2003, ApJ, 588, 65
- Shimasaku, K., et al. 2004, ApJ, 605, L93

- Spergel, D. N., Verde, L., Peiris, H. V., Komatsu, E., Nolta, M. R., Bennett, C. L., Halpern, M., Hinshaw, G., et al. 2003, ApJS, 148, 175
- Spinrad, H. 2003, "Astrophysics Update" in press, Mason, J. (Ed.) Springer Praxis Books in Astrophysics and Astronomy
- Steidel, C. C., Hamilton, D. 1992, AJ, 104, 941
- Steidel, C. C., Giavalisco, M., Dickinson, M., & Adelberger, K. L. 1996a, AJ, 112, 352
- Steidel, C. C., Giavalisco, M., Pettini, M., Dickinson, M., & Adelberger, K. L. 1996b, ApJ, 462, L17
- Steidel, C. C., Adelberger, K. L., Giavalisco, M., Dickinson, M., & Pettini, M. 1999, ApJ, 519, 1
- Steidel, C. C., Adelberger, K. L., Shapley, A. E., Pettini, M., Dickinson, M., & Giavalisco, M. 2000, ApJ, 532, 170
- Stone, R. P. S. 1996, ApJS, 107, 423
- Taniguchi, Y. 2004, Studies of Galaxies in the Young Universe with New Generation Telescope, Proceedings of Japan-German Seminar, held in Sendai, Japan, July 24-28, 2001, Eds.: N. Arimoto and W. Duschl, p. 107
- Taniguchi, Y. et al. 2003a, ApJ, 585, L97
- Taniguchi, Y. et al. 2003b, JKAS, 36, 123 (erratum 36, 283)
- Taniguchi, Y., et al. 2005, PASJ, 57, 165
- Thompson, D., & Djorgovski, S. 1995, AJ, 110, 3
- Weymann, R. J., et al. 1998, ApJ, 505, L95
- Williams, R. E., et al. 1996, AJ, 112, 1335
- Williams, R. E., et al. 2000, AJ, 120, 2735
- Wolf, C., Meisenheimer, K., Rix, H.-W., Borch, A., Dye, S., Kleinheinrich, M. 2003a, A&A, 401, 73
- Wolf, C., Wisotzki, L., Borch, A., Dye, S., Kleinheinrich, M., Meisenheimer, K. 2003b, A&A, 408, 499
- Yagi , M., Kashikawa, N., Sekiguchi, M., Doi, M., Yasuda, N., Shimasaku, K., & Okamura, S. 2002, AJ, 123, 66
- Yahata, N., Lanzetta, K. M., Turnshek, D. A., & Oke, J. B. 2000, ApJ, 538, 493
- Yan, H., Windhorst, R. A. 2004, ApJ, 612, L93

**Table 4.** Properties of LAE candidates

ID	$EW_{\text{obs}}$	$EW_{\text{rest}}$	$f_{\text{Ly}\alpha}$	$L_{\text{Ly}\alpha}$	$L_{\nu}(UV)$	$M_{UV}$	$SFR_{\text{Ly}\alpha}$	$SFR_{UV}$
	(Å)	(Å)	(erg s $^{-1}$ cm $^{-2}$ )	(erg s $^{-1}$ )	(erg s $^{-1}$ Hz $^{-1}$ )	(mag)	( $M_{\odot}$ yr $^{-1}$ )	( $M_{\odot}$ yr $^{-1}$ )
IA527								
7048	112.7	26.0	6.97E-17	6.95E+42	1.32E+29	-21.2	6.3	18.4
7988	509.4	117.5	3.96E-17	3.95E+42	1.65E+28	-18.9	3.6	2.3
9442	89.5	20.6	2.56E-17	2.56E+42	6.10E+28	-20.4	2.3	8.5
9620	484.4	111.7	2.17E-17	2.17E+42	9.56E+27	-18.4	2.0	1.3
11523	284.2	65.6	3.62E-17	3.61E+42	2.71E+28	-19.5	3.3	3.8
11538	397.5	91.7	3.61E-17	3.60E+42	1.93E+28	-19.1	3.3	2.7
13069	212.6	49.0	2.92E-17	2.91E+42	2.92E+28	-19.6	2.6	4.1
15427	989.4	228.2	2.77E-17	2.76E+42	5.96E+27	-17.8	2.5	0.8
15823	333.6	76.9	2.73E-17	2.72E+42	1.74E+28	-19.0	2.5	2.4
17533	330.0	76.1	3.28E-17	3.27E+42	2.12E+28	-19.2	3.0	3.0
19286	412.9	95.2	3.18E-17	3.17E+42	1.64E+28	-18.9	2.9	2.3
27691	1926.8	444.4	4.14E-17	4.13E+42	4.58E+27	-17.6	3.8	0.6
28584	112.8	26.0	2.21E-17	2.20E+42	4.17E+28	-20.0	2.0	5.8
28996	254.9	58.8	5.38E-17	5.37E+42	4.50E+28	-20.0	4.9	6.3
29083	292.7	67.5	2.33E-17	2.32E+42	1.70E+28	-19.0	2.1	2.4
37812	174.3	40.2	2.94E-17	2.93E+42	3.60E+28	-19.8	2.7	5.0
38785	182.3	42.0	2.75E-17	2.74E+42	3.21E+28	-19.7	2.5	4.5
41668	336.0	77.5	2.52E-17	2.52E+42	1.60E+28	-18.9	2.3	2.2
44636	159.5	36.8	2.64E-17	2.64E+42	3.53E+28	-19.8	2.4	4.9
47969	520.4	120.0	1.27E-16	1.27E+43	5.21E+28	-20.2	11.6	7.3
49443	432.4	99.7	2.36E-17	2.35E+42	1.16E+28	-18.6	2.1	1.6
51844	536.8	123.8	3.78E-17	3.77E+42	1.50E+28	-18.9	3.4	2.1
54027	181.6	41.9	3.42E-17	3.41E+42	4.02E+28	-19.9	3.1	5.6
55020	558.4	128.8	2.53E-17	2.52E+42	9.64E+27	-18.4	2.3	1.4
55100	316.0	72.9	2.53E-17	2.52E+42	1.71E+28	-19.0	2.3	2.4
55848	984.6	227.1	1.04E-16	1.03E+43	2.24E+28	-19.3	9.4	3.1
57223	632.3	145.8	2.78E-17	2.77E+42	9.36E+27	-18.3	2.5	1.3
57844	175.1	40.4	2.75E-17	2.74E+42	3.34E+28	-19.7	2.5	4.7
59074	689.7	159.1	2.36E-17	2.36E+42	7.30E+27	-18.1	2.1	1.0
59405	204.7	47.2	5.80E-17	5.78E+42	6.04E+28	-20.4	5.3	8.5
60224	319.9	73.8	3.52E-17	3.51E+42	2.34E+28	-19.3	3.2	3.3
60455	154.8	35.7	3.17E-17	3.16E+42	4.36E+28	-20.0	2.9	6.1
60664	259.9	59.9	2.20E-17	2.19E+42	1.80E+28	-19.1	2.0	2.5

**Table 4.** (Continued.)

ID	$EW_{\text{obs}}$	$EW_{\text{rest}}$	$f_{\text{Ly}\alpha}$	$L_{\text{Ly}\alpha}$	$L_{\nu}(UV)$	$M_{UV}$	$SFR_{\text{Ly}\alpha}$	$SFR_{UV}$
	(Å)	(Å)	(erg s $^{-1}$ cm $^{-2}$ )	(erg s $^{-1}$ )	(erg s $^{-1}$ Hz $^{-1}$ )	(mag)	( $M_{\odot}$ yr $^{-1}$ )	( $M_{\odot}$ yr $^{-1}$ )
63293	228.1	52.6	2.27E-17	2.27E+42	2.12E+28	-19.2	2.1	3.0
69085	478.3	110.3	2.12E-17	2.11E+42	9.44E+27	-18.3	1.9	1.3
70551	236.5	54.5	3.78E-17	3.77E+42	3.41E+28	-19.7	3.4	4.8
71679	297.5	68.6	5.03E-17	5.02E+42	3.61E+28	-19.8	4.6	5.0
72094	107.3	24.8	2.09E-17	2.08E+42	4.15E+28	-19.9	1.9	5.8
72647	610.5	140.8	4.07E-17	4.05E+42	1.42E+28	-18.8	3.7	2.0
74055	687.6	158.6	2.97E-17	2.96E+42	9.21E+27	-18.3	2.7	1.3
74299	695.1	160.3	2.50E-17	2.50E+42	7.67E+27	-18.1	2.3	1.1
75353	499.8	115.3	3.30E-17	3.29E+42	1.41E+28	-18.8	3.0	2.0
77460	188.5	43.5	2.78E-17	2.78E+42	3.15E+28	-19.6	2.5	4.4
78162	152.7	35.2	7.24E-17	7.23E+42	1.01E+29	-20.9	6.6	14.2
80388	700.2	161.5	2.92E-17	2.91E+42	8.89E+27	-18.3	2.6	1.2
81380	124.5	28.7	2.35E-17	2.34E+42	4.02E+28	-19.9	2.1	5.6
82145	290.3	67.0	2.58E-17	2.58E+42	1.90E+28	-19.1	2.3	2.7
82756	692.1	159.6	4.31E-17	4.30E+42	1.33E+28	-18.7	3.9	1.9
83157	391.4	90.3	9.34E-17	9.32E+42	5.09E+28	-20.2	8.5	7.1
86220	240.8	55.5	2.34E-17	2.33E+42	2.07E+28	-19.2	2.1	2.9
87141	319.6	73.7	5.82E-17	5.80E+42	3.88E+28	-19.9	5.3	5.4
87553	489.7	112.9	5.07E-17	5.06E+42	2.21E+28	-19.3	4.6	3.1
88785	170.3	39.3	2.41E-17	2.40E+42	3.01E+28	-19.6	2.2	4.2
89485	196.1	45.2	2.59E-17	2.58E+42	2.82E+28	-19.5	2.4	3.9
89896	1722.7	397.3	2.95E-17	2.95E+42	3.65E+27	-17.3	2.7	0.5
90874	362.4	83.6	3.97E-17	3.96E+42	2.33E+28	-19.3	3.6	3.3
94639	850.1	196.1	3.57E-17	3.56E+42	8.95E+27	-18.3	3.2	1.3
94941	1062.3	245.0	2.69E-17	2.68E+42	5.39E+27	-17.7	2.4	0.8
95272	665.4	153.4	2.44E-17	2.43E+42	7.80E+27	-18.1	2.2	1.1
96625	227.3	52.4	2.90E-17	2.89E+42	2.72E+28	-19.5	2.6	3.8
99496	667.9	154.0	3.53E-17	3.52E+42	1.12E+28	-18.5	3.2	1.6
100145	426.9	98.4	3.34E-17	3.33E+42	1.67E+28	-19.0	3.0	2.3
101147	379.6	87.5	2.28E-17	2.27E+42	1.28E+28	-18.7	2.1	1.8
102766	341.3	78.7	2.79E-17	2.78E+42	1.74E+28	-19.0	2.5	2.4
IA574								
6580	124.7	26.4	2.99E-17	3.88E+42	7.23E+28	-20.6	3.5	10.1
10969	381.4	80.7	8.44E-17	1.09E+43	6.68E+28	-20.5	10.0	9.4
11379	420.0	88.9	2.86E-17	3.71E+42	2.06E+28	-19.2	3.4	2.9

**Table 4.** (Continued.)

ID	$EW_{\text{obs}}$	$EW_{\text{rest}}$	$f_{\text{Ly}\alpha}$	$L_{\text{Ly}\alpha}$	$L_{\nu}(UV)$	$M_{UV}$	$SFR_{\text{Ly}\alpha}$	$SFR_{UV}$
	(Å)	(Å)	(erg s $^{-1}$ cm $^{-2}$ )	(erg s $^{-1}$ )	(erg s $^{-1}$ Hz $^{-1}$ )	(mag)	( $M_{\odot}$ yr $^{-1}$ )	( $M_{\odot}$ yr $^{-1}$ )
13034	796.8	168.7	2.57E-17	3.33E+42	9.74E+27	-18.4	3.0	1.4
21251	895.4	189.6	2.93E-17	3.80E+42	9.88E+27	-18.4	3.5	1.4
22223	352.1	74.6	2.81E-17	3.64E+42	2.41E+28	-19.4	3.3	3.4
25092	311.1	65.9	2.59E-17	3.36E+42	2.51E+28	-19.4	3.1	3.5
34695	390.0	82.6	6.87E-17	8.90E+42	5.31E+28	-20.2	8.1	7.4
36987	805.4	170.5	3.08E-17	4.00E+42	1.16E+28	-18.6	3.6	1.6
45242	388.8	82.3	2.84E-17	3.69E+42	2.21E+28	-19.3	3.4	3.1
46603	1243.6	263.3	1.24E-16	1.61E+43	3.00E+28	-19.6	14.6	4.2
51420	247.0	52.3	3.62E-17	4.70E+42	4.43E+28	-20.0	4.3	6.2
53464	225.6	47.8	3.96E-17	5.13E+42	5.29E+28	-20.2	4.7	7.4
53930	265.3	56.2	5.29E-17	6.86E+42	6.02E+28	-20.4	6.2	8.4
54185	307.9	65.2	2.71E-17	3.51E+42	2.65E+28	-19.5	3.2	3.7
55740	285.8	60.5	2.68E-17	3.48E+42	2.83E+28	-19.5	3.2	4.0
55786	286.1	60.6	2.78E-17	3.60E+42	2.93E+28	-19.6	3.3	4.1
57174	505.4	107.0	2.88E-17	3.73E+42	1.72E+28	-19.0	3.4	2.4
58770	316.0	66.9	3.65E-17	4.73E+42	3.48E+28	-19.8	4.3	4.9
65463	184.0	39.0	2.95E-17	3.82E+42	4.84E+28	-20.1	3.5	6.8
65839	152.8	32.3	2.65E-17	3.44E+42	5.23E+28	-20.2	3.1	7.3
66933	383.0	81.1	2.61E-17	3.38E+42	2.05E+28	-19.2	3.1	2.9
68446	258.9	54.8	2.85E-17	3.69E+42	3.32E+28	-19.7	3.4	4.6
69065	1450.1	307.0	2.95E-17	3.82E+42	6.14E+27	-17.9	3.5	0.9
71041	219.1	46.4	5.18E-17	6.72E+42	7.14E+28	-20.5	6.1	10.0
72707	1092.7	231.4	2.91E-17	3.78E+42	8.05E+27	-18.2	3.4	1.1
73613	343.1	72.6	7.85E-17	1.02E+43	6.90E+28	-20.5	9.3	9.7
74326	135.7	28.7	2.47E-17	3.20E+42	5.50E+28	-20.3	2.9	7.7
75127	204.0	43.2	4.09E-17	5.30E+42	6.05E+28	-20.4	4.8	8.5
75930	893.4	189.2	4.23E-17	5.49E+42	1.43E+28	-18.8	5.0	2.0
76201	364.5	77.2	5.06E-17	6.56E+42	4.19E+28	-20.0	6.0	5.9
77116	291.9	61.8	3.21E-17	4.17E+42	3.32E+28	-19.7	3.8	4.7
78959	1189.9	251.9	6.17E-17	8.00E+42	1.57E+28	-18.9	7.3	2.2
79754	6840.6	1448.4	3.61E-17	4.69E+42	1.59E+27	-16.4	4.3	0.2
82975	1087.8	230.3	2.81E-17	3.64E+42	7.80E+27	-18.1	3.3	1.1
85436	769.0	162.8	2.86E-17	3.71E+42	1.12E+28	-18.5	3.4	1.6
90651	1303.0	275.9	3.41E-17	4.42E+42	7.91E+27	-18.1	4.0	1.1
91865	255.4	54.1	4.47E-17	5.80E+42	5.29E+28	-20.2	5.3	7.4

**Table 4.** (Continued.)

ID	$EW_{\text{obs}}$	$EW_{\text{rest}}$	$f_{\text{Ly}\alpha}$	$L_{\text{Ly}\alpha}$	$L_{\nu}(UV)$	$M_{UV}$	$SFR_{\text{Ly}\alpha}$	$SFR_{UV}$
	(Å)	(Å)	(erg s $^{-1}$ cm $^{-2}$ )	(erg s $^{-1}$ )	(erg s $^{-1}$ Hz $^{-1}$ )	(mag)	( $M_{\odot}$ yr $^{-1}$ )	( $M_{\odot}$ yr $^{-1}$ )
96523	426.4	90.3	3.23E-17	4.20E+42	2.29E+28	-19.3	3.8	3.2
99338	637.8	135.1	2.92E-17	3.79E+42	1.38E+28	-18.8	3.5	1.9
IA598								
10519	262.0	53.1	3.34E-17	4.94E+42	4.58E+28	-20.1	4.5	6.4
12390	110.9	22.5	2.61E-17	3.86E+42	8.46E+28	-20.7	3.5	11.8
13299	214.0	43.4	3.27E-17	4.83E+42	5.50E+28	-20.3	4.4	7.7
27435	547.0	110.9	3.92E-17	5.80E+42	2.58E+28	-19.4	5.3	3.6
33977	265.3	53.8	2.49E-17	3.68E+42	3.37E+28	-19.7	3.4	4.7
37912	181.9	36.9	3.17E-17	4.69E+42	6.27E+28	-20.4	4.3	8.8
53728	302.9	61.4	2.73E-17	4.03E+42	3.24E+28	-19.7	3.7	4.5
53761	169.6	34.4	3.11E-17	4.61E+42	6.60E+28	-20.4	4.2	9.2
55275	388.4	78.7	3.42E-17	5.05E+42	3.16E+28	-19.7	4.6	4.4
58192	175.6	35.6	2.97E-17	4.39E+42	6.07E+28	-20.4	4.0	8.5
59826	1162.9	235.7	2.93E-17	4.33E+42	9.06E+27	-18.3	3.9	1.3
60845	149.3	30.3	2.84E-17	4.20E+42	6.84E+28	-20.5	3.8	9.6
64675	299.1	60.6	4.34E-17	6.42E+42	5.22E+28	-20.2	5.8	7.3
65983	383.9	77.8	3.20E-17	4.73E+42	3.00E+28	-19.6	4.3	4.2
80344	570.6	115.7	3.61E-17	5.34E+42	2.28E+28	-19.3	4.9	3.2
81987	261.4	53.0	2.70E-17	3.99E+42	3.71E+28	-19.8	3.6	5.2
85081	381.6	77.3	2.85E-17	4.21E+42	2.69E+28	-19.5	3.8	3.8
87226	321.7	65.2	3.88E-17	5.74E+42	4.34E+28	-20.0	5.2	6.1
89279	224.3	45.5	8.82E-17	1.30E+43	1.41E+29	-21.3	11.9	19.8
92776	578.8	117.3	2.48E-17	3.66E+42	1.54E+28	-18.9	3.3	2.2
IA624								
15802	1150.5	224.7	3.76E-17	6.21E+42	1.36E+28	-18.7	5.7	1.9
16965	283.3	55.3	3.03E-17	5.00E+42	4.45E+28	-20.0	4.5	6.2
18537	196.6	38.4	2.54E-17	4.19E+42	5.38E+28	-20.2	3.8	7.5
18866	398.9	77.9	2.32E-17	3.82E+42	2.42E+28	-19.4	3.5	3.4
26804	230.9	45.1	2.48E-17	4.10E+42	4.48E+28	-20.0	3.7	6.3
30834	666.1	130.1	2.72E-17	4.49E+42	1.70E+28	-19.0	4.1	2.4
31226	125.6	24.5	2.84E-17	4.69E+42	9.43E+28	-20.8	4.3	13.2
33170	1607.5	314.0	3.84E-17	6.34E+42	9.96E+27	-18.4	5.8	1.4
38991	128.9	25.2	2.88E-17	4.75E+42	9.29E+28	-20.8	4.3	13.0
40098	532.4	104.0	4.31E-17	7.11E+42	3.37E+28	-19.7	6.5	4.7

**Table 4.** (Continued.)

ID	$EW_{\text{obs}}$	$EW_{\text{rest}}$	$f_{\text{Ly}\alpha}$	$L_{\text{Ly}\alpha}$	$L_{\nu}(UV)$	$M_{UV}$	$SFR_{\text{Ly}\alpha}$	$SFR_{UV}$
	(Å)	(Å)	(erg s $^{-1}$ cm $^{-2}$ )	(erg s $^{-1}$ )	(erg s $^{-1}$ Hz $^{-1}$ )	(mag)	( $M_{\odot}$ yr $^{-1}$ )	( $M_{\odot}$ yr $^{-1}$ )
52800	489.3	95.6	2.30E-17	3.80E+42	1.96E+28	-19.1	3.5	2.7
53168	465.8	91.0	2.28E-17	3.76E+42	2.04E+28	-19.2	3.4	2.9
56258	670.8	131.0	3.31E-17	5.45E+42	2.05E+28	-19.2	5.0	2.9
57053	355.1	69.4	2.55E-17	4.21E+42	2.99E+28	-19.6	3.8	4.2
59547	178.6	34.9	2.73E-17	4.50E+42	6.36E+28	-20.4	4.1	8.9
60562	207.4	40.5	2.20E-17	3.64E+42	4.43E+28	-20.0	3.3	6.2
61041	228.5	44.6	2.81E-17	4.64E+42	5.12E+28	-20.2	4.2	7.2
61778	459.3	89.7	2.39E-17	3.95E+42	2.17E+28	-19.2	3.6	3.0
62001	220.5	43.1	3.51E-17	5.79E+42	6.63E+28	-20.5	5.3	9.3
63836	492.5	96.2	6.35E-17	1.05E+43	5.37E+28	-20.2	9.5	7.5
68957	116.2	22.7	2.34E-17	3.86E+42	8.38E+28	-20.7	3.5	11.7
69429	195.6	38.2	2.86E-17	4.71E+42	6.08E+28	-20.4	4.3	8.5
83307	922.2	180.1	5.19E-17	8.56E+42	2.34E+28	-19.3	7.8	3.3
93077	1171.9	228.9	3.99E-17	6.58E+42	1.42E+28	-18.8	6.0	2.0
99353	553.8	108.2	4.03E-17	6.66E+42	3.03E+28	-19.6	6.1	4.2
99689	571.6	111.6	3.58E-17	5.91E+42	2.61E+28	-19.4	5.4	3.7
IA651								
18239	656.0	122.7	4.16E-17	7.79E+42	3.13E+28	-19.6	7.1	4.4
18481	597.6	111.8	3.90E-17	7.30E+42	3.22E+28	-19.7	6.6	4.5
18929	181.8	34.0	2.19E-17	4.10E+42	5.94E+28	-20.3	3.7	8.3
56248	241.2	45.1	3.30E-17	6.18E+42	6.75E+28	-20.5	5.6	9.4
58954	459.4	85.9	6.68E-17	1.25E+43	7.18E+28	-20.6	11.4	10.1
60304	267.7	50.1	2.70E-17	5.06E+42	4.98E+28	-20.1	4.6	7.0
61944	657.8	123.0	2.48E-17	4.64E+42	1.86E+28	-19.1	4.2	2.6
62565	340.9	63.8	2.82E-17	5.29E+42	4.09E+28	-19.9	4.8	5.7
65736	465.6	87.1	2.41E-17	4.51E+42	2.55E+28	-19.4	4.1	3.6
68104	410.6	76.8	2.65E-17	4.96E+42	3.18E+28	-19.7	4.5	4.5
70056	254.0	47.5	2.48E-17	4.64E+42	4.81E+28	-20.1	4.2	6.7
87781	173.1	32.4	2.44E-17	4.57E+42	6.96E+28	-20.5	4.2	9.7
95072	1327.7	248.3	4.26E-17	7.98E+42	1.58E+28	-18.9	7.3	2.2
96758	312.4	58.4	2.97E-17	5.56E+42	4.69E+28	-20.1	5.1	6.6
97673	369.1	69.0	3.06E-17	5.73E+42	4.09E+28	-19.9	5.2	5.7
98943	160.0	29.9	2.32E-17	4.35E+42	7.17E+28	-20.5	4.0	10.0
IA679								

**Table 4.** (Continued.)

ID	$EW_{\text{obs}}$	$EW_{\text{rest}}$	$f_{\text{Ly}\alpha}$	$L_{\text{Ly}\alpha}$	$L_{\nu}(UV)$	$M_{UV}$	$SFR_{\text{Ly}\alpha}$	$SFR_{UV}$
	(Å)	(Å)	(erg s $^{-1}$ cm $^{-2}$ )	(erg s $^{-1}$ )	(erg s $^{-1}$ Hz $^{-1}$ )	(mag)	( $M_{\odot}$ yr $^{-1}$ )	( $M_{\odot}$ yr $^{-1}$ )
9065	476.5	85.4	2.29E-17	4.87E+42	2.81E+28	-19.5	4.4	3.9
11843	268.6	48.1	7.76E-17	1.65E+43	1.69E+29	-21.5	15.0	23.6
16415	492.9	88.3	3.56E-17	7.56E+42	4.22E+28	-20.0	6.9	5.9
18878	615.4	110.3	2.55E-17	5.41E+42	2.42E+28	-19.4	4.9	3.4
19202	606.7	108.7	2.97E-17	6.30E+42	2.86E+28	-19.6	5.7	4.0
24769	398.4	71.4	5.62E-17	1.19E+43	8.24E+28	-20.7	10.9	11.5
33768	198.0	35.5	2.12E-17	4.50E+42	6.25E+28	-20.4	4.1	8.8
46786	265.8	47.6	2.48E-17	5.27E+42	5.46E+28	-20.2	4.8	7.6
47730	174.4	31.2	2.01E-17	4.27E+42	6.74E+28	-20.5	3.9	9.4
52102	458.6	82.2	3.19E-17	6.77E+42	4.06E+28	-19.9	6.2	5.7
57794	583.6	104.5	2.60E-17	5.51E+42	2.60E+28	-19.4	5.0	3.6
60173	265.6	47.6	3.59E-17	7.61E+42	7.88E+28	-20.6	6.9	11.0
62116	327.7	58.7	3.45E-17	7.31E+42	6.14E+28	-20.4	6.7	8.6
64479	273.6	49.0	2.20E-17	4.67E+42	4.70E+28	-20.1	4.3	6.6
65576	137.0	24.6	2.74E-17	5.80E+42	1.17E+29	-21.1	5.3	16.3
74655	624.1	111.8	2.25E-17	4.77E+42	2.10E+28	-19.2	4.3	2.9
89098	469.6	84.1	3.14E-17	6.66E+42	3.90E+28	-19.9	6.1	5.5
IA709								
8190	154.1	26.5	2.02E-17	4.83E+42	9.00E+28	-20.8	4.4	12.6
13683	978.3	168.0	2.59E-17	6.20E+42	1.82E+28	-19.1	5.6	2.5
18701	321.4	55.2	2.21E-17	5.30E+42	4.73E+28	-20.1	4.8	6.6
31658	267.5	45.9	2.40E-17	5.75E+42	6.17E+28	-20.4	5.2	8.6
33815	177.6	30.5	2.78E-17	6.66E+42	1.08E+29	-21.0	6.1	15.1
34592	272.0	46.7	2.37E-17	5.68E+42	6.00E+28	-20.4	5.2	8.4
38261	309.8	53.2	2.18E-17	5.21E+42	4.83E+28	-20.1	4.7	6.8
51167	225.2	38.7	2.28E-17	5.45E+42	6.94E+28	-20.5	5.0	9.7
55557	176.5	30.3	2.45E-17	5.88E+42	9.56E+28	-20.9	5.3	13.4
59617	460.3	79.0	6.84E-17	1.64E+43	1.02E+29	-20.9	14.9	14.3
66451	171.7	29.5	1.96E-17	4.68E+42	7.83E+28	-20.6	4.3	11.0
72647	907.7	155.9	2.43E-17	5.83E+42	1.84E+28	-19.1	5.3	2.6
80850	286.9	49.3	2.02E-17	4.84E+42	4.84E+28	-20.1	4.4	6.8
83599	946.8	162.6	2.81E-17	6.73E+42	2.04E+28	-19.2	6.1	2.9
84928	809.3	139.0	4.08E-17	9.76E+42	3.46E+28	-19.8	8.9	4.8

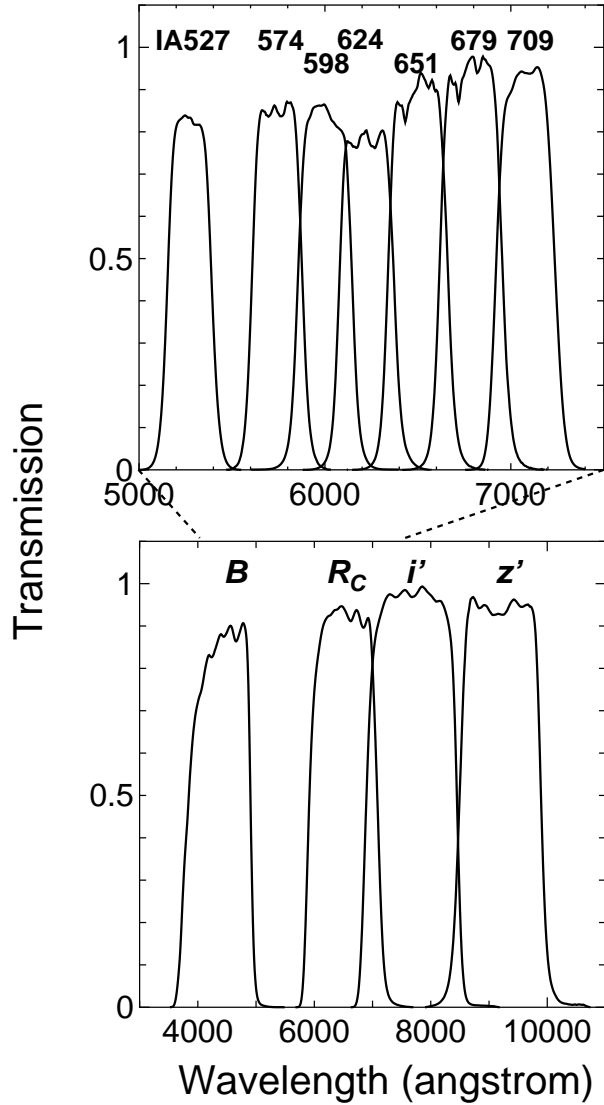


**Fig. 1.** Transmission curves of the filters used in this study. Lower panel shows the four broad band filters and upper panel shows a close up for the seven IA filters.

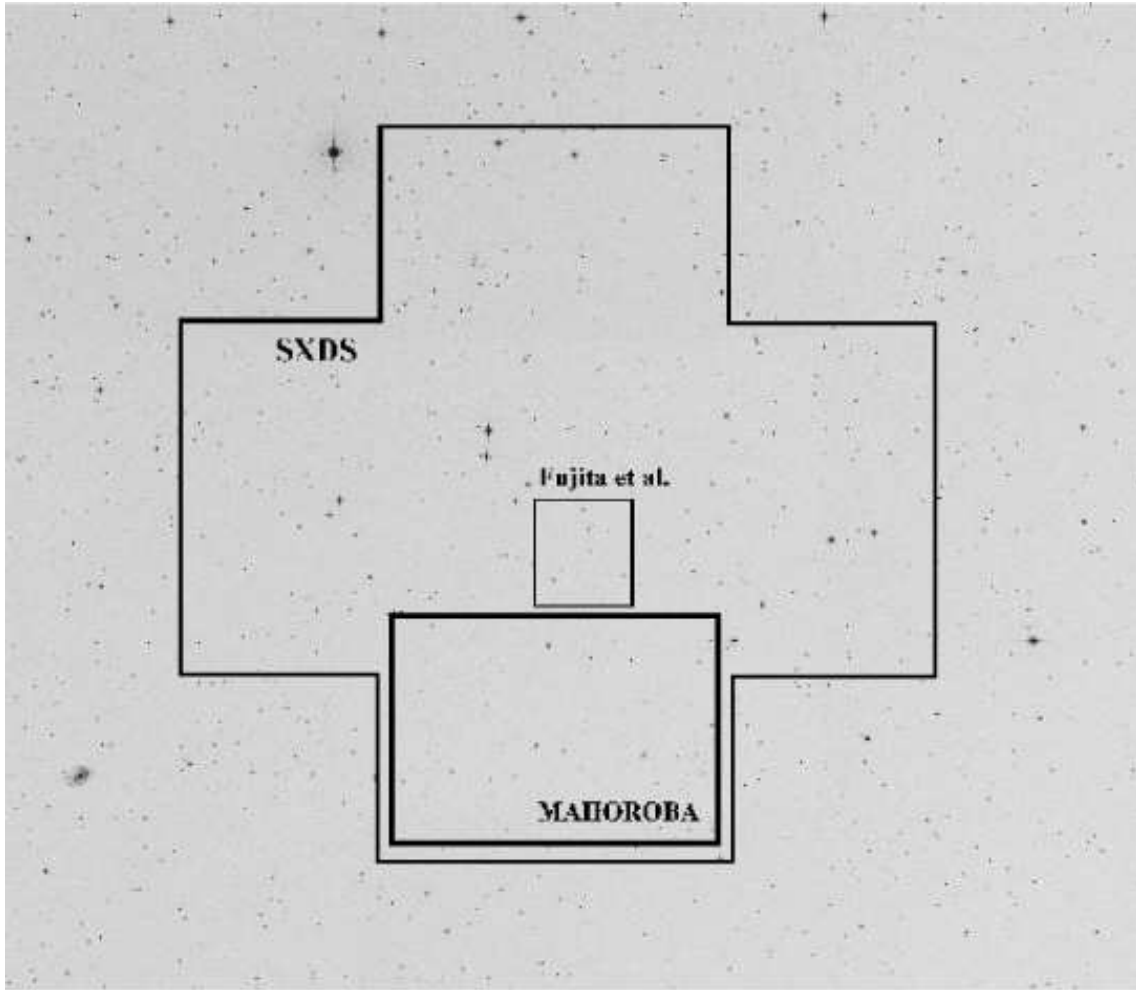


**Fig. 2.** The entire field of view of the SXDS field. Our MAHOROBA field ( $34.^{\circ}71 \times 27.^{\circ}20$ ) is a sky area in the southern part of the SXDS field while that of Fujita et al. (2003a) is located in the central part( $13.^{\circ}7 \times 13.^{\circ}7$ ).

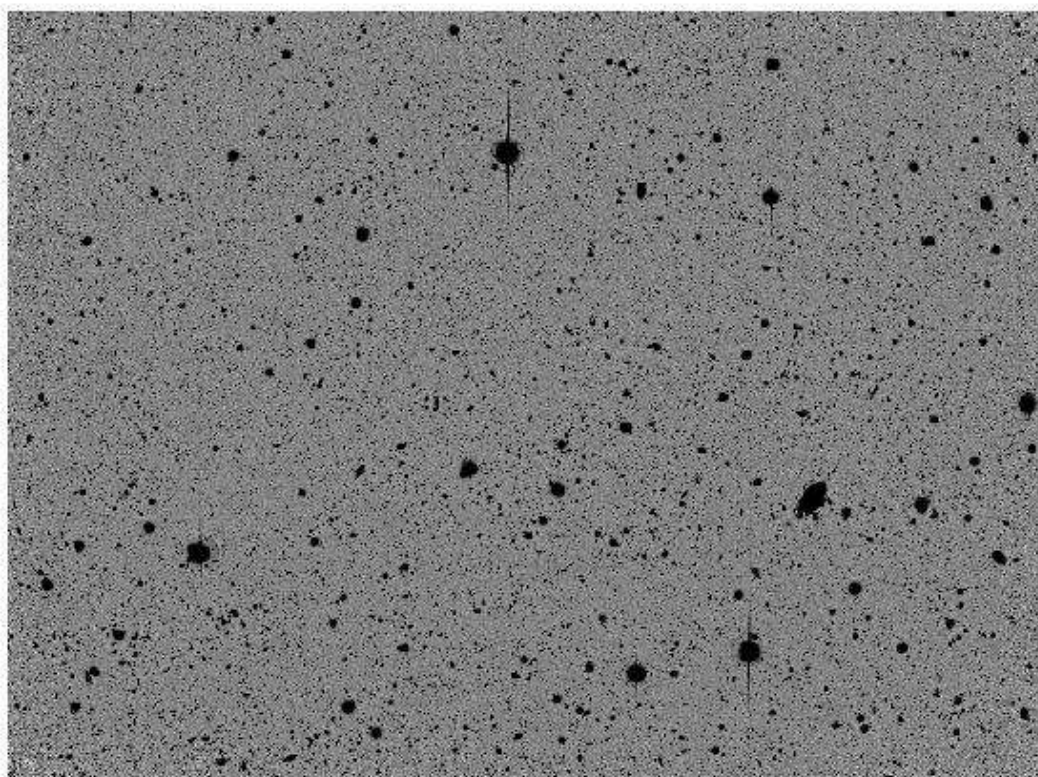


**Fig. 3.** The stacked image obtained with the seven IA filters.

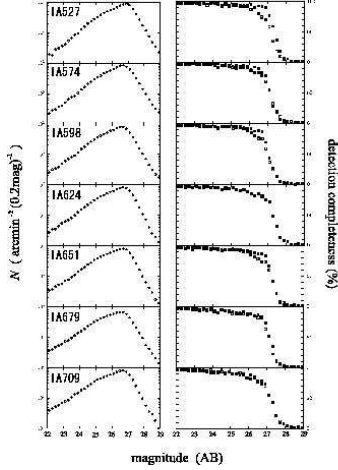


**Fig. 4.** Left : Number counts per  $\text{arcmin}^2$  in 0.2 mag bin. Right : The detection completeness of artificial galaxies using the simulation. Filled squares show the results from the data sets using the exponential law. Open squares show that of the de Vaucouleurs law.

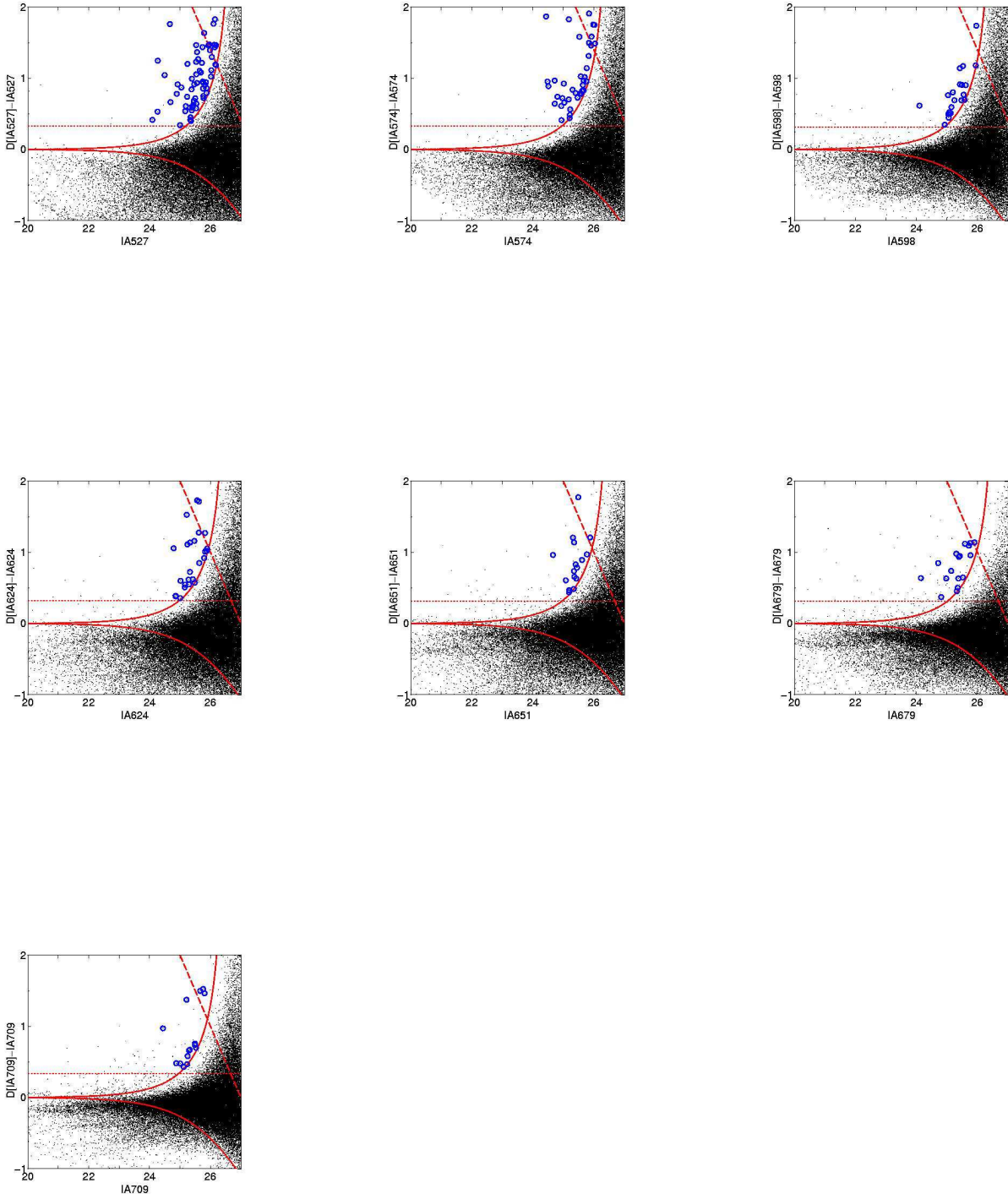


**Fig. 5.** Color-magnitude diagrams for objects with  $IA < 27$  at each IA filter. Red dotted horizontal line corresponds to the criterion of  $EW_{\text{rest}} = 20\text{\AA}$ . Red dashed line corresponds to  $3\sigma$  of  $D[\text{IA}]$ . Red solid curve corresponds to  $3\sigma$  of  $D[\text{IA}] - IA$ . Blue open circles show LAE candidates.

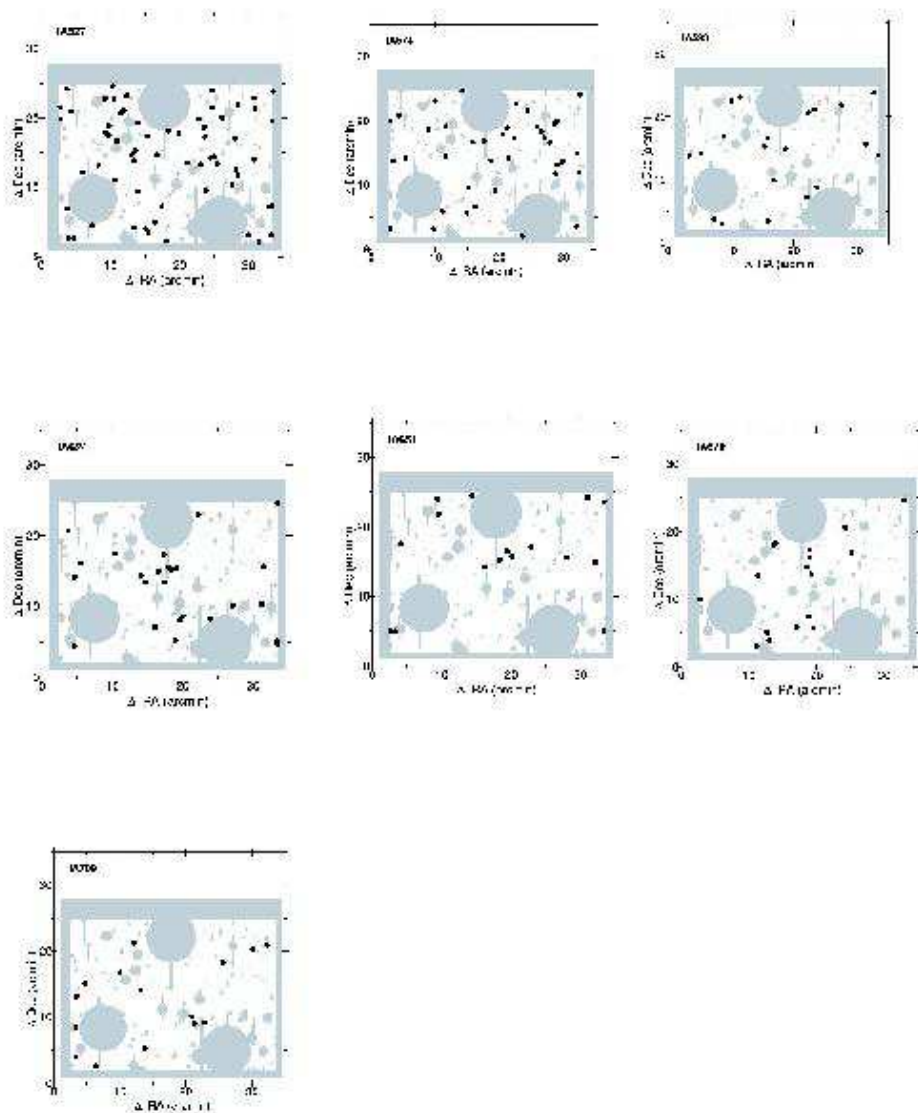


**Fig. 6.** The spatial distributions of LAE candidates. The gray shadow show the masked area. The three large area in these figure are masked for the starlight contamination.

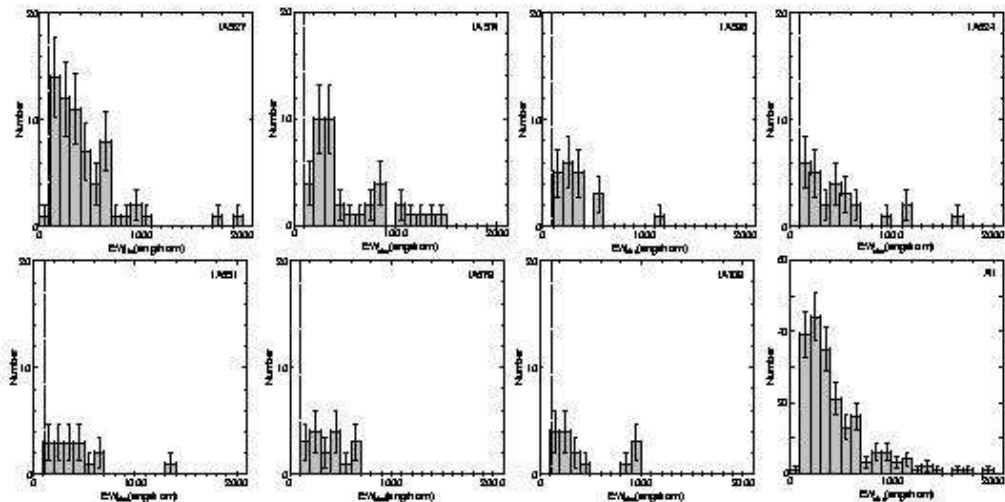


**Fig. 7.**  $EW_{\text{obs}}$  distribution of LAE candidates found in each IA-excess catalog. Vertical line in each panel corresponds to  $\text{mag}(EW_{\text{rest}} = 20 \text{\AA})$ . In the panel for  $IA574$ , one large  $EW_{\text{obs}}$  objects is not shown; its equivalent width is  $EW_{\text{obs}} = 6840 \text{\AA}$ .

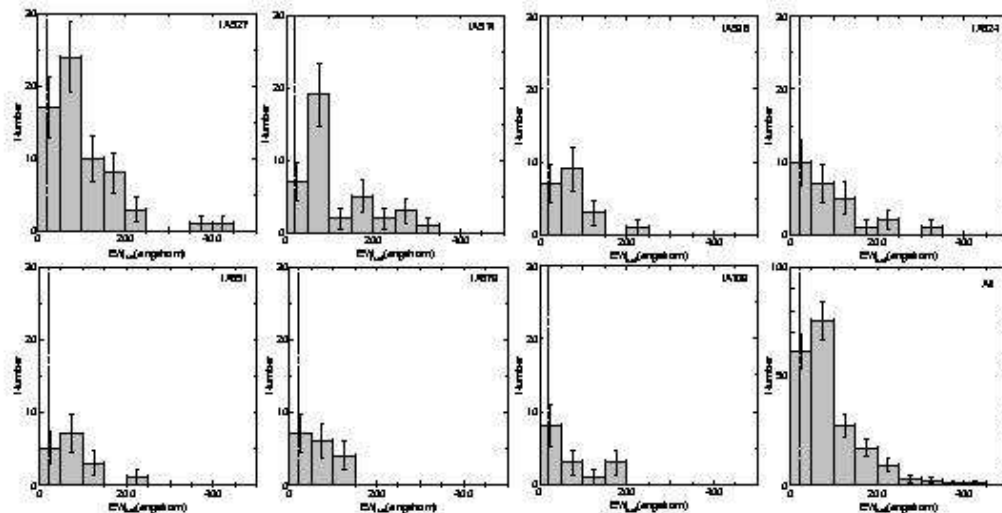


**Fig. 8.**  $EW_0$  distribution of LAE candidates in each IA-excess catalog. Vertical line in each panel corresponds to  $mag(EW_{rest} = 20\text{\AA})$ . In the panel for IA574, one large  $EW_{obs}$  objects is not shown; its equivalent width is  $EW_{obs} = 1448\text{\AA}$ .

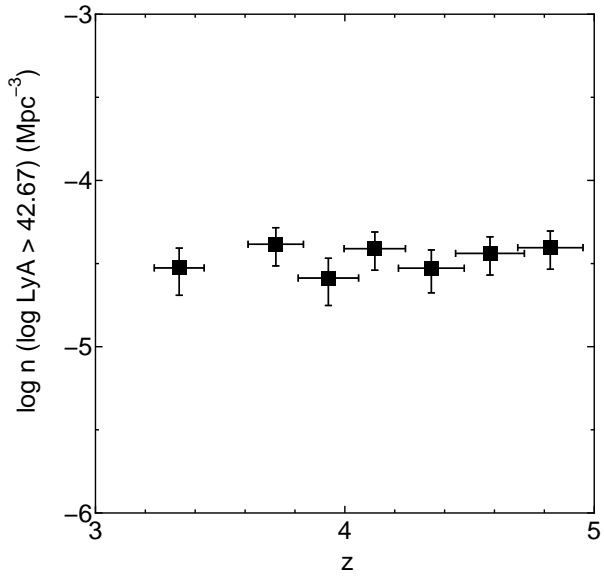


**Fig. 9.** Number densities of LAE candidates are shown as a function of redshift. The horizon error bar simply shows the redshift coverage of each IA filter.

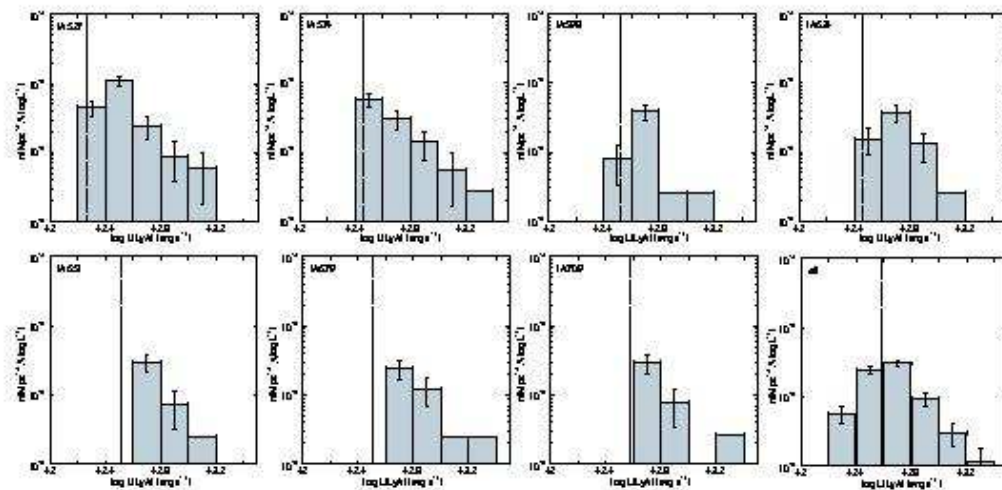


**Fig. 10.** Luminosity distributions of LAE candidates in each IA-excess catalog. The lower right panel shows the results for all LAE candidates. The vertical lines show the limit of  $L(\text{Ly}\alpha)$  at each filter.

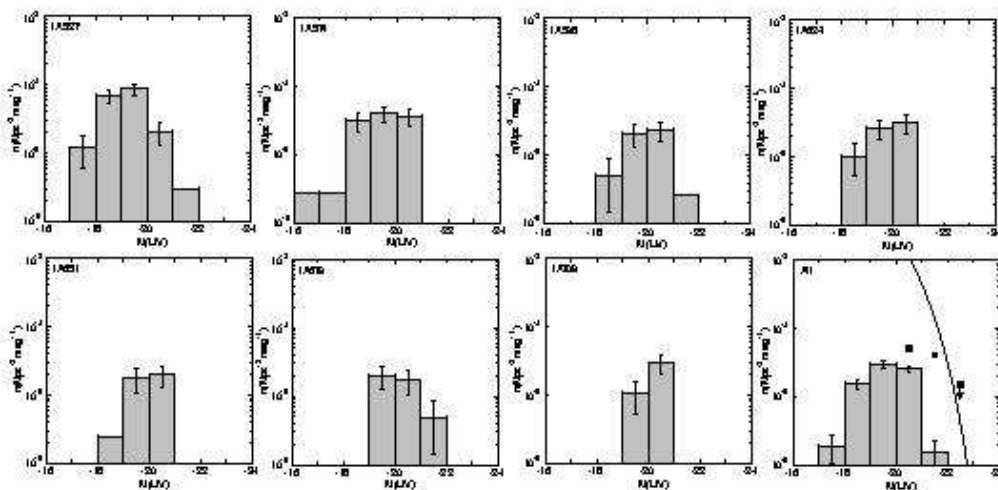


**Fig. 11.** Luminosity distributions of the absolute *UV* magnitude for LAE candidates;  $1\sigma$  errors are also shown. Filled squares in the lower-right panel show the results for  $z \sim 5.7$  LAEs (Hu et al. 2004). Solid line in the same panel show the UV luminosity function for LBGs at  $z \sim 4$  (Ouchi et al. 2004).

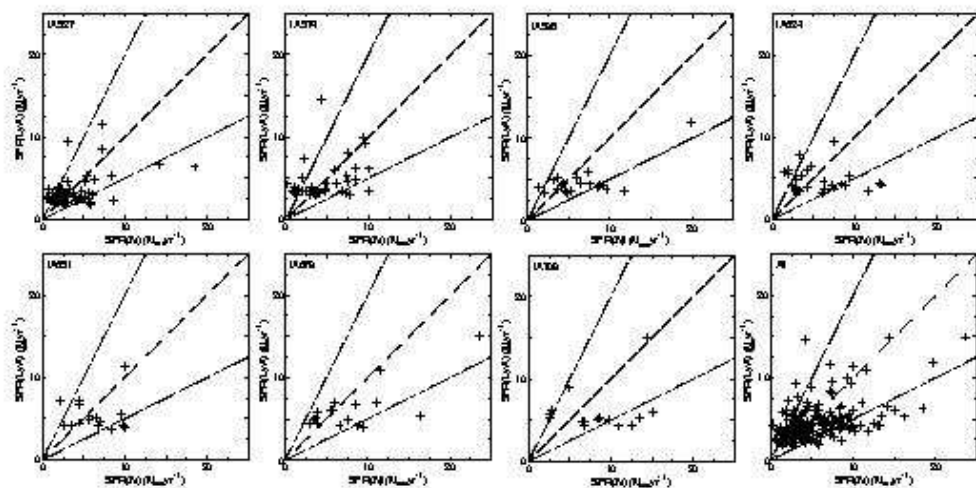


**Fig. 12.** Comparison between  $SFR(\text{Ly}\alpha)$  and  $SFR(\text{UV})$  for LAEs in each IA-excess catalog. The following relations are also shown; 1)  $SFR(\text{Ly}\alpha) = SFR(\text{UV})$  (dashed line), 2)  $SFR(\text{Ly}\alpha) = 2 \times SFR(\text{UV})$  (dotted line), 3)  $SFR(\text{Ly}\alpha) = 0.5 \times SFR(\text{UV})$  (dash-dotted line), and 4) the fitting result (solid line). The lower-right panel shows the results for all LAE43

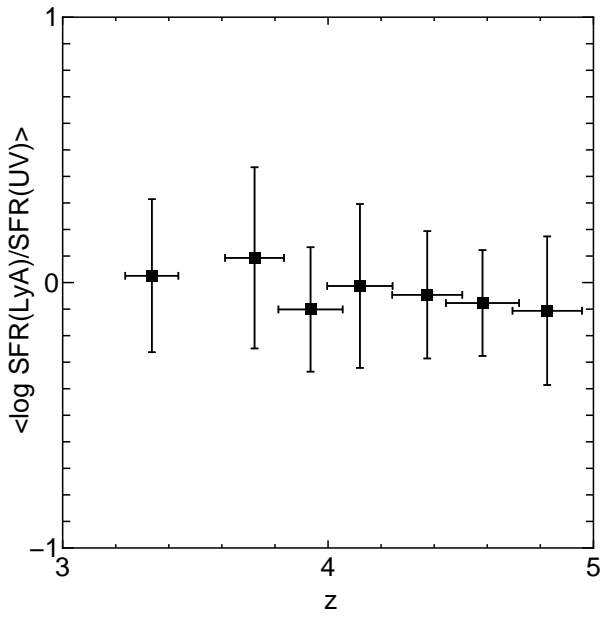


**Fig. 13.** The average ratio of  $SFR(\text{Ly}\alpha)$  to  $SFR(\text{UV})$  is shown As a function of redshift. Our results are shown by filled squares.

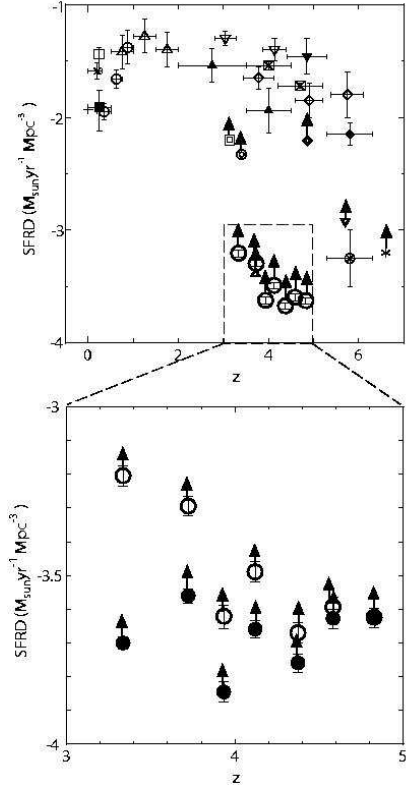


**Fig. 14.** Upper panel shows the cosmic evolution of the star formation rate density as a function of redshift. Our results are shown by large open circles (for all LAEs). Results of previous LAE surveys are also shown; The data sources are Taniguchi et al. (2005, asterisk), Ouchi et al. (2004, double diamond), Fujita et al. (2003a, double triangle), Cowie & Hu (1998, double circle), Kudritzki et al. (2000, double square). All the data above show the lower limit of SFRD. We therefore show these data with the up-arrow. The data using Lyman break method are shown by the points with error of *SFRD*. Those based on LBGs are also shown; Steidel et al. (2000, open inverse triangles), Madau et al. (1998, filled triangles), Connolly et al. (1997, open triangles), Lilly et al. (1996, open circles), Iwata et al. (2003, filled inverse triangle), Giavalisco et al. (2003, open diamonds). The other data sources of SFRD are Gallego et al. (1996, plus), Tresse & Maddox (1998, cross), Fujita et al. (2003b, open square), Treyer et al. (1998, filled square). Lower panel shows the cosmic evolution of the star formation rate density as a function of redshift. We compare the lower limit of SFRD derived from our data. The large open circles show the sum of SFRD for all LAEs and the large filled circles show the sum of SFRD for LAEs with  $\log(\text{Ly}\alpha) > 42.67$ .

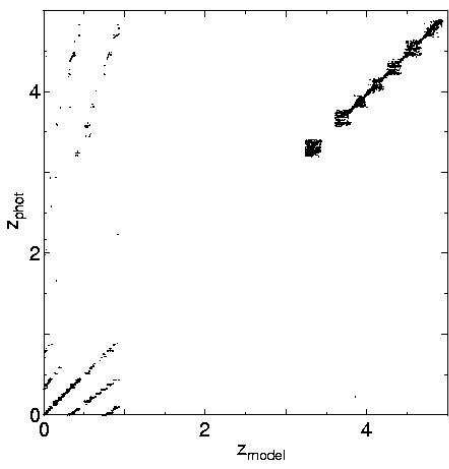


**Fig. 15.** Comparison between  $z_{\text{model}}$  and  $z_{\text{phot}}$  for simulated catalogs selected as emission-line galaxies.